Influence of Vortical Structure on Flame Acceleration in Hydrogen-Air, Methane-Air, and Hydrogen-Methane/Air Blend

Samira Kia

Thesis submitted to the University of Ottawa
in partial fulfillment of the requirements for the
Master of Applied Science in Mechanical Engineering

Faculty of Engineering
Department of Mechanical Engineering
University of Ottawa

Abstract

Following the ignition of a flame in a duct, the characteristics of the flame-driven flow play an important role in the propagation and acceleration of the flame. When bluff body obstacles are present in the duct, vortical structures are formed in the flow downstream of the obstacle. The subsequent interaction of the flame with these vortices is believed to generate substantial flame deformation and acceleration. In the present study, we investigate the deformation of the flame resulting from its interaction with these vortices. The experiments were performed in stoichiometric hydrogen-air, methane-air, and an equimolar blend of hydrogen and methane at ambient conditions.

Experiments were conducted in a thin, rectangular shock tube, with a rectangular obstacle positioned within it. The shock tube was initially filled with the mixtures at atmospheric pressure. A planar flame was then ignited at the closed end of the shock tube using a long wire ignition technique and propagated toward the open end. The high Reynolds number of the flow ahead of the flame resulted in flow separation at the leading edge of the obstacle, forming a vortical structure. Following the entrainment of the flame into the vortex, the flame surface area increased, resulting in the acceleration of the flame-driven flow. The evolution of the flame was visualized using high-speed direct shadowgraph and Z-type Schlieren. The pressure evolution was measured using pressure transducers placed along the top and bottom walls of the shock tube.

The measured evolution of the flame speed and overpressure inside the shock tube highlights the higher reactivity and flame acceleration of the hydrogen-air flame compared to the flames propagating in methane-air and equimolar hydrogen-methane blend with air. To facilitate a better comparison of the propagating flames, the pressure and velocity measurements obtained from the experiments are expressed in a non-dimensional form. This approach effectively eliminates the dependence on the distinct laminar burning velocities of each mixture. Hydrogen, with its characteristic thin flame structure, is less affected by the turbulent features formed behind the obstacle than mixtures containing methane. These mixtures show a much larger increase in flame surface area and wrinkled structures because their flame times are longer than the characteristic time of the vortical structure. Consequently, they exhibit a higher normalized pressure peak compared to the hydrogen mixture. To compare the normalized overpressure between methane-air and equimolar mixtures, in the equimolar flame, due to the relatively shorter flame time and an increase in the concentration of hydrogen in the positive curvatures of the flame front, the amount of local quenching induced by turbulence is reduced. As a result, the equimolar mixture records a higher normalized pressure than the methane mixture.

In the second set of experiments, two parallel mirrors positioned at a 45-degree angle are installed on the top and bottom walls of the shock tube to visualize the third dimension of the flame propagating along the shock tube. This method is applied for the first time in this study, and the shadowgraph technique is used to capture 3D flame propagation. It is observed that the mixtures with a Lewis number below unity (hydrogen and the equimolar mixtures) show more 3D effects compared to the methane mixture. These two flames tend to incline along the width of the shock tube, and this behavior intensifies when the flames get entrained into the vortical structures and accelerate.

Acknowledgements

I am deeply grateful to my supervisor, Dr. Matei I. Radulescu, for giving me the opportunity to work under his supervision and guidance in the Detonation and Reactive Dynamics Laboratory. Being part of Dr. Radulescu's research group has allowed me to gain valuable experience; his mentorship has been pivotal to my professional development and learning.

This research is supported by funding from FM Global, whose contribution is gratefully acknowledged and warmly appreciated.

My sincerest gratitude to Kevin Cheevers for his help and guidance in performing the experiments, which have been beneficial for this study.

I would like to express my profound appreciation to my parents and my husband for their unwavering support and inspiration throughout my graduate studies.

Table of Contents

List of Tables vii

List of Figures viii

1 Introduction 1

1.1 Problem Definition . . . 1

1.2 Flame Front Instabilities . . . 3

1.2.1 Diffusional-thermal instability . . . 3

1.2.2 Hydrodynamic instability . . . 4

1.2.3 Buoyancy-driven instability . . . 5

1.2.4 Kelvin-Helmholtz instability . . . 6

1.3 Background and Motivation . . . 7

1.4 The Current Study . . . 9

2 Experimental Setup 11

2.1 Shock tube Apparatus . . . 11

2.2 Visualization . . . 12

2.2.1 The Edgerton Shadowgraph technique . . . 13

2.2.2 The Z-type Schlieren technique . . . 14

2.2.3 Three-dimensional visualization setup . . . 15

2.2.4 Test Gases . . . 18

3 Flame Vortex Entrainment **21**

3.1 Hydrogen-Air mixture 21

3.2 Equimolar Methane/Hydrogen-Air mixture 22

3.3 Methane-Air mixture 22

3.4 Characteristic scales for data reduction 34

3.5 Experimental Scaling 36

3.6 Flame area amplification in the mixtures 38

4 Three-Dimensional visualization **40**

4.1 3rd Dimension Visualization 40

4.2 Flame Tip Velocity 50

4.3 Effect of Lewis number on flame deformation in the 3rd dimension 54

5 Conclusion **57**

References **60**

List of Tables

2.1 Composition of test gases for the experiments 20

3.1 Mixtures composition and flame properties at atmospheric conditions (P= 101.2 kPa, T= 295 K). 35

3.2 Downstream vortex diameter and velocity in three mixtures 39

4.1 Effective Lewis number formulation for bi-component fuels [1] 55

List of Figures

1.1 Evolution of the flame and vortical structure, visualized using Schlieren(The contrasts of the flame and the vortex are enhanced to more clearly illustrate their evolution) . . . 2

1.2 Schematic showing the mechanism of diffusional-thermal cellular instability [2]. 4

1.3 Schematic showing the mechanism of hydrodynamic instability [3] . . . 6

1.4 Evolution of the flame, visualized using shadowgraph. Times are shown above each frame and t=0 is the time when the flame ignites . . . 10

1.5 Three-dimensional flame evolution, visualized using shadowgraph. Times are shown above each frame and t=0 is the time when the flame ignites. . . 10

2.1 Diagrams of the experimental setup and shock tube configuration . . . 13

2.2 General schematic of piston stroke in formation of vortex ring [4] . . . 14

2.3 Shadowgraph technique arrangement . . . 15

2.4 Z-type Schlieren arrangement [5] . . . 16

2.5 The prism mirrors for three-dimensional visualization . . . 17

2.6 Mirrors configuration inside the shock tube for three-dimensional visualization . . . 17

2.7 The bottom mirror's visualization of the shock tube's width . . . 18

2.8 Checking the mirrors periscope functionality . . . 19

2.9 Schematic path of light beams . . . 20

3.1 Evolution of the stochiometric hydrogen-air flame visualized using shadowgraph technique. Times are shown above each frame and t=0 is the time when the flame ignites and $t' = 0$ is the moment the flame tip crosses the leading edge of the obstacle. 24

3.2 Evolution of the equimolar flame visualized using shadowgraph technique. Times are shown above each frame and t=0 is the time when the flame ignites and $t' = 0$ is the moment the flame tip crosses the leading edge of the obstacle. 25

3.3 Evolution of the methane-air flame visualized using shadowgraph technique. Times are shown above each frame and t=0 is the time when the flame ignites and $t' = 0$ is the moment the flame tip crosses the leading edge of the obstacle. 26

3.4 Evolution of the flames in the three mixtures visualized using shadowgraph technique. Times are shown above each frame and t=0 is the time when the flame ignites and $t' = 0$ is the moment the flame tip crosses the leading edge of the obstacle. 27

3.5 Evolution of the vortical structure and flame, visualized using Schlieren in hydrogen (left side) and equimolar (right side) mixtures. 28

3.6 Evolution of the flame tip velocity for hydrogen-air flame over time. Time $t = 0$ is defined as the moment when the flame tip crosses the leading edge of the obstacle. 29

3.7 Evolution of the flame tip velocity for equimolar blend-air flame over time. Time $t = 0$ is defined as the moment when the flame tip crosses the leading edge of the obstacle. 30

3.8 Evolution of the flame tip velocity for methane-air flame over time. Time t = 0 is defined as the moment when the flame tip crosses the leading edge of the obstacle. 30

3.9 Evolution of the pressure inside the shock tube for hydrogen-air flame over time. Time $t = 0$ is defined as the moment when the flame tip crosses the leading edge of the obstacle. 32

3.10 Evolution of the pressure inside the shock tube for equimolar blend-air flame over time. Time $t = 0$ is defined as the moment when the flame tip crosses the leading edge of the obstacle. 32

3.11 Evolution of the pressure inside the shock tube for methane-air flame over time. Time $t = 0$ is defined as the moment when the flame tip crosses the leading edge of the obstacle. 33

3.12 Flame-driven flow creates a multiscale turbulent structure in the presence of an obstacle downstream. 34

3.13 Scaled flame tip velocity as a function of scaled time.The time flame tip crosses the leading edge of the obstacle is represented by $t = 0$. 36

3.14 Scaled over pressure as a function of scaled time.The time flame tip crosses the leading edge of the obstacle is represented by $t = 0$. 37

4.1 Three-dimensional visualization of hydrogen-air flame evolution using shadowgraph technique. Times are shown above each frame and t=0 is the time when the flame ignites. 43

4.2 Three-dimensional visualization of equimolar blend flame evolution using shadowgraph technique. Times are shown above each frame and t=0 is the time when the flame ignites. 46

4.3 Three-dimensional visualization of methane-air flame evolution using shadowgraph technique. Times are shown above each frame and t=0 is the time when the flame ignites. 49

4.4 Three-dimensional visualization the flames evolution using shadowgraph technique. Times are shown above each frame and t=0 is the time when the flame ignites. 51

4.5 Three-dimensional visualization of the selected frames shown in a closer view. 52

4.6 Evolution of the flame tip velocity for hydrogen-air flame over time. Time $t = 0$ is defined as the moment when the flame tip crosses the leading edge of the obstacle. 53

4.7 Evolution of the flame tip velocity for blend-air flame over time. Time $t = 0$ is defined as the moment when the flame tip crosses the leading edge of the obstacle. 53

4.8 Evolution of the flame tip velocity for methane-air flame over time. Time $t = 0$ is defined as the moment when the flame tip crosses the leading edge of the obstacle. 54

4.9 Effective Lewis number formulations for H_2/C_3H_8/air flames versus H_2 fuel volumetric content [1] 56

Chapter 1

Introduction

1.1 Problem Definition

The introduction of hydrogen into the energy sector in the form of fuel blends with natural gas to reduce carbon emissions has revealed new gaps in our understanding of how these blends behave. In terms of industrial process safety, one concern is the potential for flame acceleration after accidental ignition, particularly in congested environments. Despite sharing similar burning expansion ratios, hydrogen-air and methane-air have significantly different physical properties, such as flame thickness and flame time. Methane is considered a relatively unreactive fuel, with a low burning velocity and long flame time. In contrast, hydrogen is much more reactive and burns faster.

Over the years, a considerable amount of research has been dedicated to understanding the phenomenon of flame behavior and acceleration in pure fuels such as hydrogen and hydrocarbons. However, the flame propagation characteristics of these fuel blends remain an area of uncertainty.

The dynamics of flame propagation are intricately linked to the flow field dynamics through a strong coupling between the cellular structure of the flame front, surface area changes of the flame, and the characteristics of the flame-driven flow induced by the volumetric expansion of gases across the flame. Pressure waves are generated during the build-up and advance of a flame. These pressure waves perturb the flow field ahead of the flame and create velocity and pressure gradients [6].

This would be further complicated by the presence of an obstacle in the downstream flow field, which can generate turbulence and vortical structures because of the high Reynolds

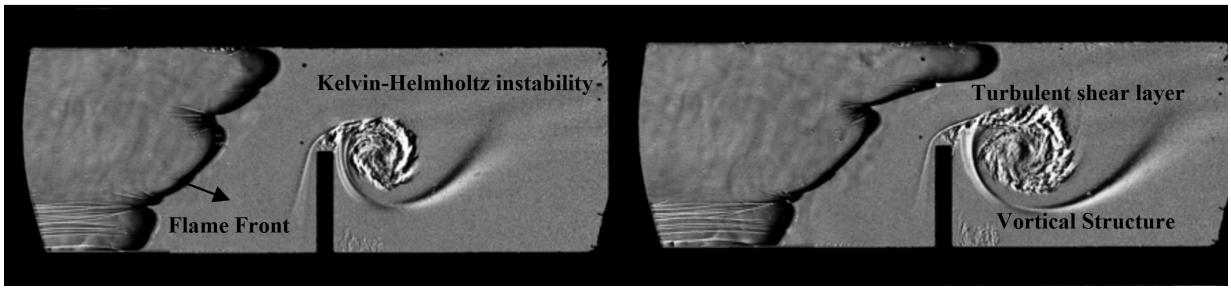

Figure 1.1: Evolution of the flame and vortical structure, visualized using Schlieren(The contrasts of the flame and the vortex are enhanced to more clearly illustrate their evolution)

number in the flow field and Kelvin-Helmholtz instability. We can see the formation of a turbulent shear layer and vortices in Figure 1.1.

The purpose of placing an obstacle in the downstream flow is to create a throat and simulate the condition near a vented explosion. As mentioned, it is important to investigate the behavior of flames from a safety standpoint.

The flame surface is deformed due to the interaction between flow dynamics and the flame front. This includes Landau–Darrieus instabilities associated with the gas expansion across the flame, Rayleigh-Taylor instabilities resulting from the misalignment of the flow pressure gradient and the density gradient across the flame, and Kelvin-Helmholtz instabilities resulting from velocity shear across slip-lines separating fluids with different velocities. Additionally, the flame is entrained through turbulent flow fields such as turbulent shear layers and eddies found downstream from the obstacle.

These dynamic phenomena each have an associated timescale that can be used to describe their interaction with the flame: those with timescales much longer than the flame time will be unable to meaningfully change the flame surface and structure, whereas those whose timescales are comparable to or smaller than the flame time will affect the structure and properties of the flame. This may penetrate into the flame sheet, stretch flame front, and may cause local quenching [7].

1.2 Flame Front Instabilities

There are three basic distinct types of phenomena that responsible for intrinsic instabilities of premixed flames: diffusional-thermal instability [8, 9], body-force (buoyancy-driven) instability and hydrodynamic instability [10, 11]. The body-force instability is the effect of acceleration in a non-inertial reference frame. Cellular flames that spontaneously take on a nonplanar shape often have structures affected most strongly by diffusional-thermal phenomena. However, body-force and hydrodynamic phenomena also play roles [3].

1.2.1 Diffusional-thermal instability

Diffusional-thermal instability mechanism can be explained by referring to Figure 1.2, where the arrows indicate directions of net fluxes of heat and species. A key element in the explanation is the fact that for large values of the Zel'dovich number (which is defined as a nondimensional measure of the temperature sensitivity of the overall reaction rate. Qualitatively, it indicates the strength of the reaction rate's dependence on the extent of the reaction completed), the burning velocity depends mainly on the local flame temperature T_f. Convexity in the reaction sheet extending toward the unburned gas serves as a local sink for reactants and a local source for heat. Increasing the rate of diffusion of the limiting reactant to the flame sheet increases the rate of heat release there and hence tends to increase the flame temperature T_f, while increasing the rate of heat conduction from the flame sheet tends to reduce T_f.

At the convex (the convex curvature toward the unburned side), the local gradients will be steepened in comparison with those of the normal flame, and the reactant and conductive flux will be increased. If the thermal diffusivity equals the diffusivity of the limiting reactant (Le $= 1$), then these increases are balanced in such a way that T_f is unchanged. However, if the thermal diffusivity is greater than mass diffusivity (Le > 1, weakly diffusing reactants), then T_f decreases at the convex. While if the thermal diffusivity is less than mass diffusivity (Le < 1, strongly diffusing reactant), then T_f increases (as a consequence of the preferential diffusion of the reactant with respect to heat), in this situation, the local increase in flame speed, associated with the increase in flame temperature T_f , causes the convex part of the flame become larger, thereby reinforce the diffusional-thermal instability for mixture with Le< 1 [3].

In two-reactant systems with $\mathrm{Le}_1 \neq \mathrm{Le}_2$, there is an additional purely diffusive effect, which is introduced as preferential diffusion of reactants. The more strongly diffusing reactant can reach the sink at the convex readily than its weakly diffusing partner. Therefore, the

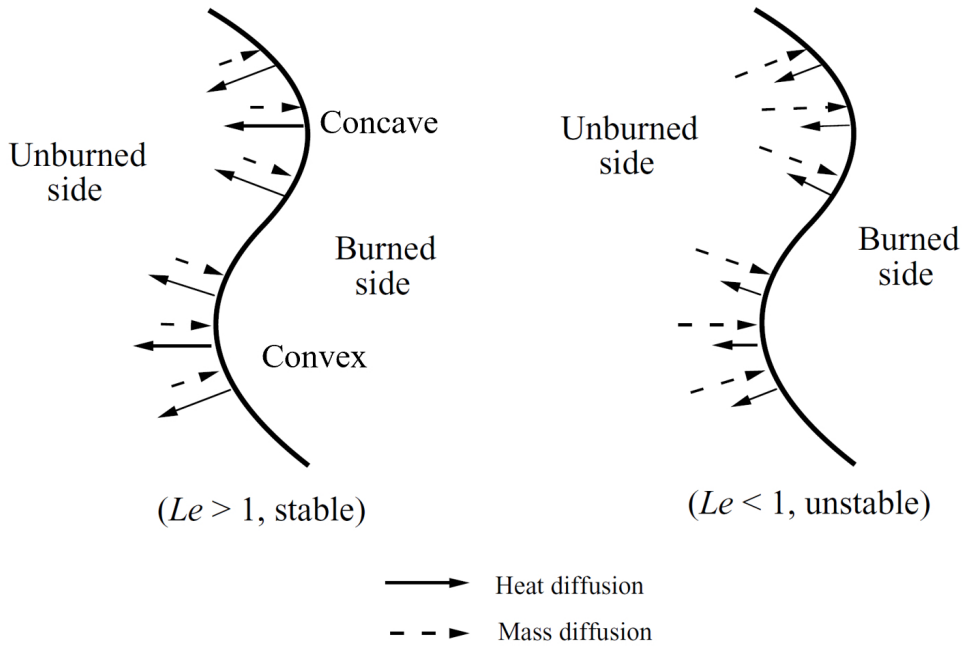

Figure 1.2: Schematic showing the mechanism of diffusional-thermal cellular instability [2].

wrinkles induce local mixture-ratio variations. Convex parts of flame are relatively enriched in the strongly diffusing reactant and concave parts of flame are consequently enriched in the weakly diffusing reactant.

These differences in reactant distribution impact the dynamics of the reaction sheet. Specifically, they affect the flame speed due to thermal effects. In near-stoichiometric mixtures, these influences are comparable in magnitude to the effects of diffusive-thermal interactions. If the limiting component is relatively strongly diffusing, then the mixture-ratio variations intensify instability, Variations in the mixture-ratio of a weakly diffusing limiting reactant have a stabilizing effect. At stoichiometric conditions for a mixture that has its maximum normal burning velocity at stoichiometry, convex parts can tend to be suppressed, and concave parts can tend to be amplified by mixture-ratio variations [3].

1.2.2 Hydrodynamic instability

Hydrodynamic instability, also known as the Landau–Darrieus instability, is caused by the density jump across the flame. In this analysis, Landau and Darrieus neglect body forces

and treat the entire flame simply as a discontinuity in density that propagates normal to itself at a constant speed S_L. By considering flame propagation toward more dense unburned gas, this thermal expansion across the flame causes the planar deflagration become unstable. Referring to Figure 1.3, it is seen that continuity of the tangential component of velocity across a flame element require the streamlines to be deflected toward the local normal to the flame sheet. This causes a stream tube of initial area equal to A (which must be the same far upstream and far downstream where the perturbations vanish there) to be larger at the flame than far away if the sheet is convex toward the unburned gas. In incompressible flow, the area increase causes a velocity decrease.

Since a flame sheet perturbation with an upstream flame displacement (F) geometrically must have a curvature convex toward the unburned gas, it encounters a decreased fluid velocity and therefore (as propagating at its normal speed) will tend to move even farther upstream. Conversely, a downstream flame displacement results in stream-tube contraction and, therefore, a tendency toward further displacement toward downstream [3].

In other words, for the convex segment of the flame, the widening of the streamlines causes the flow to slow down. However, since the flame speed remains unaffected as specified, the local velocities of the approach flow and the flame can no longer balance each other, hence resulting in further advancement of this flame segment into the unburned mixture. A similar argument for the concave segment shows that it will further recede into the burned side [2].

Also, it is observed that small wrinkles grow more rapidly than large wrinkles. The growth rate is inversely proportional to the wavelength of disturbances, small wrinkles grow more rapidly than large wrinkles. As the wavelength decreases and approaches the thickness of the flame, it is no longer permissible to treat the flame as a discontinuity. Even for wavelengths on the order of 10 to 100 times the deflagration thickness, diffusive and thermal effects within the flame may cause the flame speed to depend appreciably on the flame shape and the local flow field [3].

1.2.3 Buoyancy-driven instability

The buoyancy-driven instability is commonly known as the Rayleigh–Taylor instability. A fluid is buoyantly unstable when a less-dense fluid is beneath a more-dense one. Therefore, an upwardly propagating flame is buoyantly unstable because the denser, unburned mixture is over the lighter, burned product, while the converse holds for a downwardly propagating flame. Furthermore, an accelerating flame experiences a body force directed from the unburned to the burned mixtures [2].

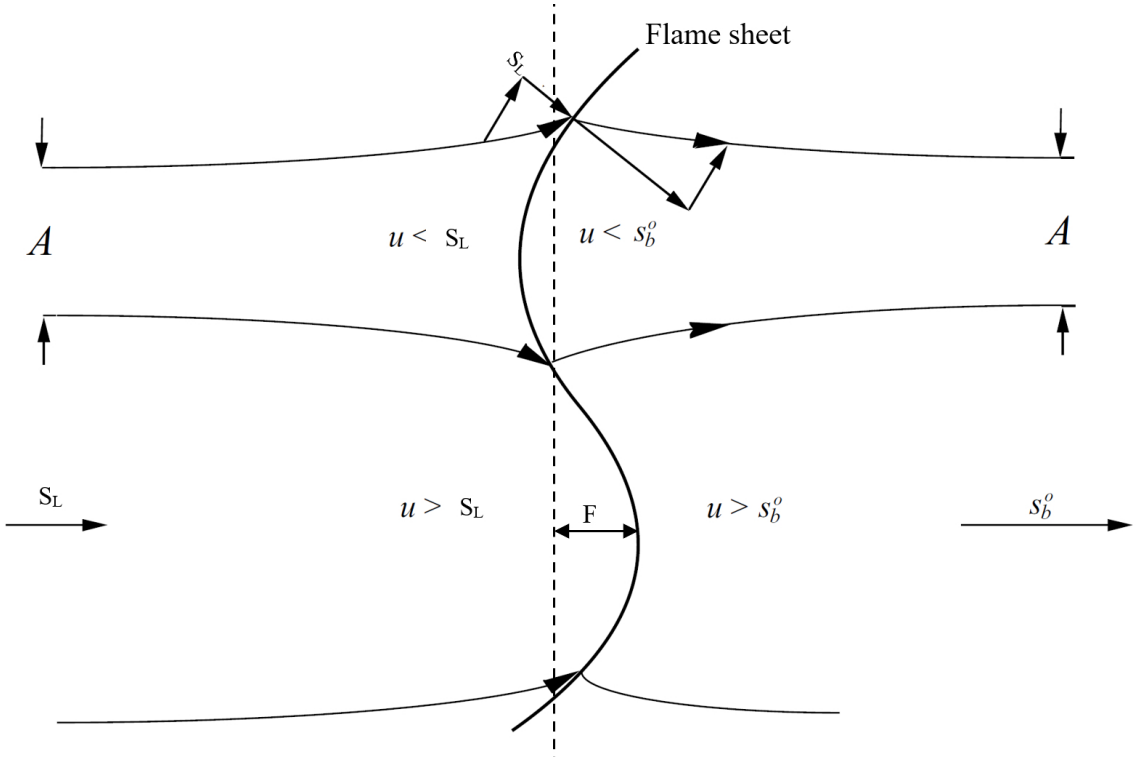

Figure 1.3: Schematic showing the mechanism of hydrodynamic instability [3]

The acceleration of a flame sheet generates effects like those produced by body forces. In a non-inertial coordinate system that moves with the flame, an effective body force appears because of flame acceleration. Thus a flame acceleration in the direction of its motion is equivalent to a body force directed from the unburned to the burned gas. A body-force instability is therefore associated with flame acceleration [3].

1.2.4 Kelvin-Helmholtz instability

While this instability is not categorized as a flame front instability, it is discussed in this section due to the presence of obstacle in downstream flow and the generation of vortical structures. In this study, Kelvin-Helmholtz instability significantly impacts the flame-driven flow, flame propagation, and the evolution of pressure inside the shock tube.

This instability occurs when there is a velocity shear in a single continuous fluid or a velocity difference across the interface between two fluids. It arises due to the interplay between

the velocity difference of the fluids. When the velocity difference is significant enough, it can overcome the stabilizing effects of surface tension or density gradients, leading to the growth of disturbances at the interface. These disturbances can lead to the formation of characteristic wave-like patterns, vortices, and eventually break into turbulence.

1.3 Background and Motivation

Johansen and Ciccarelli investigated the flame acceleration process in an obstructed square cross-section channel. They tracked the formation of vortex downstream of each obstacle. The size of the vortex increases with time until it reaches the channel wall and completely spans the distance between adjacent obstacles. The development of the recirculation zones governs the combustion in the gap between obstacles. Oscillations in centerline flame velocity are due to the acceleration and deceleration of the unburned gas as it flows through each obstacle. It was found that initial rates of flame acceleration were higher for large blockage ratios due to enhanced turbulence production and increased bulk burning rate associated with larger flame areas [12]. Roberts et al. studied the effects of flame curvature for flames with Lewis numbers less than and above unity. For flames with Lewis numbers less than unity, where there is a strong positive flame curvature, the reaction rate is enhanced. These results agree with the analysis of Law [2] who showed how the reaction rate should increase where the local burned gas temperature is enhanced by the thermodiffusive effects. For flames with Lewis numbers greater than unity, positive flame curvature causes a reduction in the reaction rate [13].

Shi et al. studied the effects of differential diffusion of hydrogen (H_2) on flame structure in laminar premixed fuel-lean H_2/CH_4/air polyhedral flames. The results reveal that the positively curved troughs have significantly higher H_2 mole fraction compared to the negatively curved cusps, due to the respective focusing/defocusing effect of curvature on highly diffusive H_2. Consequently, the local equivalence ratio and temperature in trough regions are higher than those of cusps. In the polyhedral H_2/CH_4/air flames with 79% H_2, the peak local equivalence ratio of trough is 12% higher than the equivalence ratio in the inlet mixture. With the increase of H_2 content 50%, 68% and 79% (by volume), equivalence ratio and C/H-atom ratio differences between trough and cusp are enlarged. At an intermediate temperature of 1200 K, the X_{H_2} increases from cusp to trough is about 60%, 80%, and 100% in the three studied cases [14].

Dejoan et al. performed the numerical study of the propagation of isobaric premixed flames in narrow channels [15]. They investigated the effects of thermal expansion, Lewis number and heat losses in a planar channel geometry. Like the results presented by Kurdyumov

in [16], in narrow channels, for mixtures with Lewis number smaller than one, symmetric and non-symmetric solutions may co-exist for the same set of parameters. It was demonstrated by means of global stability analysis that when this is the case, the non-symmetric solution is stable while the symmetric solution is usually unstable. It was proven that for Lewis numbers below one, even just slightly below, there is always a critical channel width beyond which the non-symmetric solutions appear. Based on their conclusion, at least two different kinds of instabilities/effects contribute simultaneously to the emergence of non-symmetric flames in narrow channels. The first one is the differential-diffusion instability and the second is the Landau–Darrieus instability [15].

Pizza et al. numerically studied the stabilization and dynamics of lean ($\phi = 0.5$) premixed hydrogen/air atmospheric pressure flames in mesoscale planar channels by using detailed chemistry and transport equations. Thay investigated flame propagation in different channel height $h = 2$, 4, and 7 and inflow velocities $0.3 \leq U_{\text{in}} \leq 1100\text{cm/s}$. Chaotic behavior of cellular flame structures was observed for certain values of U_{in}. Based on their results, in the $h = 2$ mm channel, chaotic oscillations were observed for inflow velocities close to the upper limit of the stability range of $100 \leq U_{\text{in}} \leq 220\text{cm/s}$, whereas in the $h = 4$ mm channel this behavior occurred close to the lower limit. Finally, for $h = 7$ mm only chaotic oscillations were observed [17, 18]. The experiments of Ju and Xu in mesoscale tubes with diameters ranging from 3 to 8 mm revealed that depending on the tube width, flow velocity, and wall thermal properties, multiple (fast and slow propagation) regimes existed for self-propagating methane–air and propane–air flames. Accompanying analysis, using 1-D detailed chemistry/transport as well as 2-D single-step chemistry thermo-diffusive models, was in qualitative agreement with the experiments [19].

Cui et al. assessed the effects of differential diffusion on the burning process for both thick (narrow channels) and thin (wide channels) of premixed flames in two-dimensional channels. A thin flame is strongly affected by the underlying flow field and may develop areas of high curvature when the effective Lewis number is reduced to sufficiently low values causing a tip-opening or a dead-space near the walls. Differential diffusion is known to influence the overall burning rate, an increase in burning rate happens when the effective Lewis number Le is lowered. Indeed, their calculations showed that the flame generates more surface area when Le is reduced, but this dependency is only significant when the flame is relatively thin, or in wide channels [20].

Galisteo et al. investigated the propagation of an isobaric premixed flame with unity fuel Lewis number between two parallel plates numerically. The plates are separated by a small distance h and considered as adiabatic. As the distance between the plates decreases, loss of momentum enhances the hydrodynamic instability in comparison with that of a freely (unconfined) propagating flame. When distance between the plates increases, flame

curvature can become important and contribute significantly to the overall propagation rate [21].

1.4 The Current Study

The objective of this thesis is to examine and compare flame acceleration and behavior when entrained into a vortical structure in three different mixtures: stoichiometric hydrogen-air, methane-air, and an equimolar blend of these two fuels. To simulate the conditions near a vented explosion, we placed an obstacle downstream of the flames and studied how these flames interact with the vortical structure behind the obstacle. Also, an important property is the pressure evolution inside the shock tube as the flames propagate.

We study this phenomenon experimentally through two sets of experiments, using a thin rectangular cross-sectioned shock tube in which a cellular flame is ignited near a closed end using a long wire ignition technique. A single rectangular obstacle is placed ahead of the flame, and the far end of the tube is opened to the ambient environment, such that the flame propagation is not restricted by a closed wall and the flame front is not affected by the reflection of waves. The evolution of the flame as it passes over the obstacle is visualized using both Schlieren photography to capture the details of the flow field and the recirculation zone behind the obstacle, and shadowgraph to visualize the flame propagation over longer distances (Figure 1.4).

The coupling between the flame-induced flow and the flame surface is quantified through measurements of experimental photographs and the evolution of pressure measured along the top and bottom walls. Dimensional analysis is conducted to identify the scales of interest, which allows us to eliminate dependence on the distinct laminar burning velocities of these mixtures and study other properties of the flames. Differences between mixtures are associated with the response of the flames to various instabilities and the turbulent structure resulting from the flow field ahead of the flames.

To gain a deeper understanding of flame behavior, we designed a new experimental setup to visualize the three-dimensional propagation of flames. These experiments aimed to investigate the flame structure in the third dimension along the shock tube's width (Figure 1.5).

In these experiments, two parallel mirrors positioned at a 45-degree angle were installed on the top and bottom walls of the shock tube to visualize the third dimension of the flame propagating along width of the shock tube. This method is applied for the first time in this study, and the shadowgraph technique is used to capture 3D flame propagation.

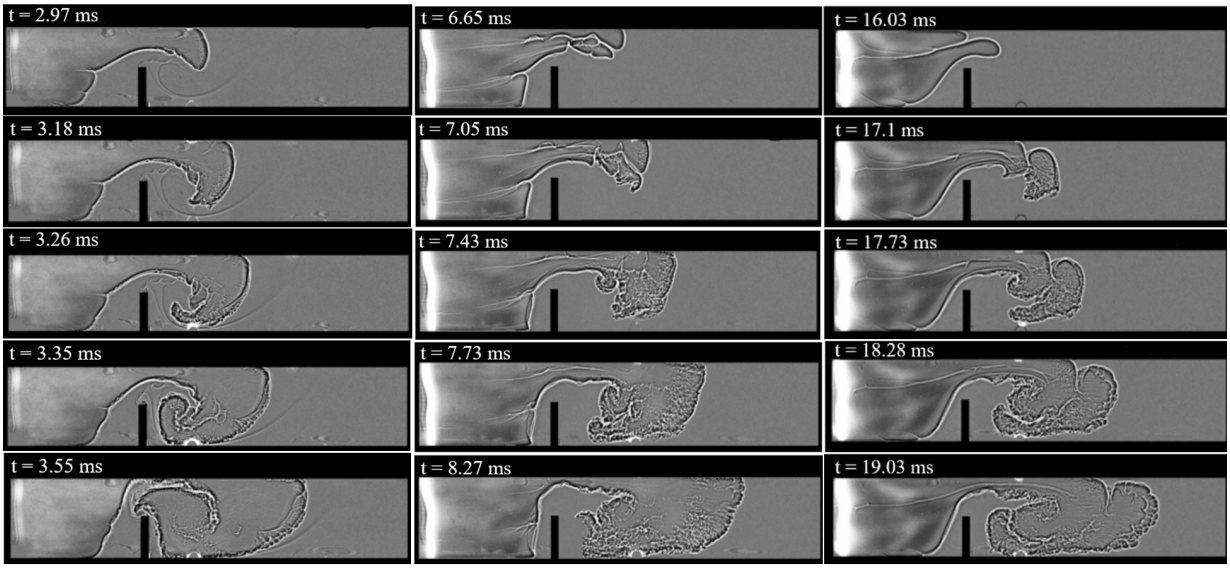

Figure 1.4: Evolution of the flame, visualized using shadowgraph. Times are shown above each frame and t=0 is the time when the flame ignites

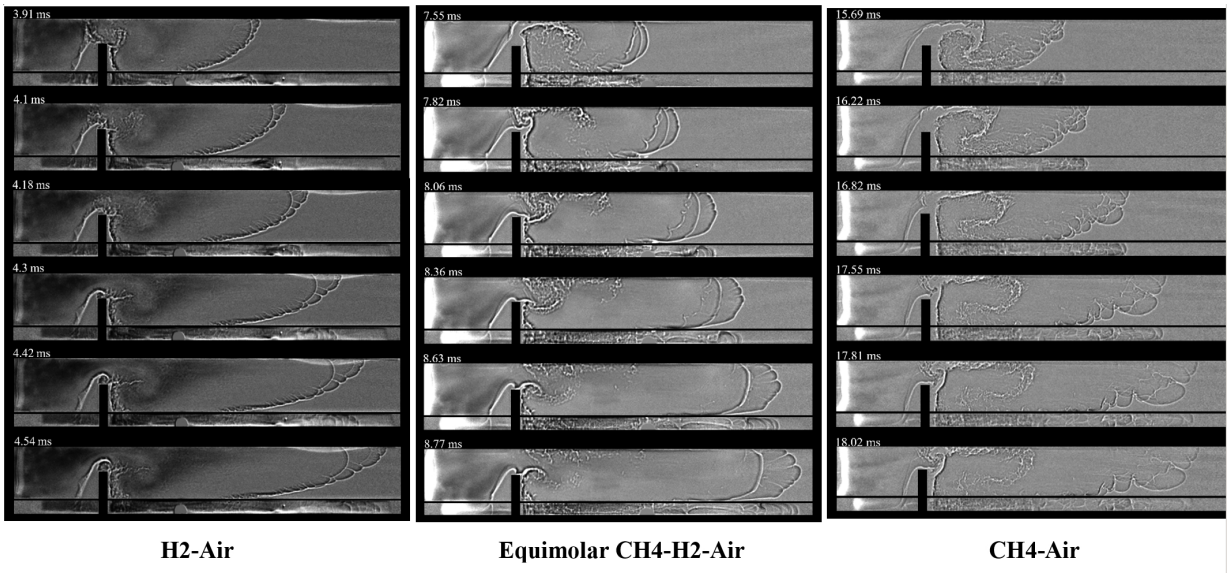

Figure 1.5: Three-dimensional flame evolution, visualized using shadowgraph. Times are shown above each frame and t=0 is the time when the flame ignites.

Chapter 2

Experimental Setup

Following the ignition of a flame in a duct, the characteristics of the flame-driven flow play an important role in the flame's propagation and acceleration. When an obstacle is presented in the duct, vortical structures form in the flow downstream of the obstacle. The subsequent interaction of the flame with these vortices is believed to generate substantial flame deformation and acceleration.

In this study, the interaction between the flame and the vortices, as well as the resulting flame acceleration and deformation, was investigated experimentally. The experiments were performed using three mixtures: stoichiometric hydrogen-air, methane-air, and an equimolar blend of hydrogen and methane with air, all at ambient conditions. The purpose of placing an obstacle downstream of the flames was to simulate conditions near a vented explosion and examine the evolution of flame pressure and velocity within the shock tube.

In this chapter, the facilities and methods used to generate the flames, along with the 2D and 3D visualizations, are discussed.

2.1 Shock tube Apparatus

The experiments were conducted using a thin 19 mm high-pressure shock tube with a height of 102 mm and a length of 630 mm, as illustrated in Figure 2.1. The shock tube in these experiments consisted of one section which was equipped with standard 19 mm tempered glasses to allow optical access. The pressure evolution was measured using pressure transducers placed along the top and bottom walls of the shock tube.

Prior to each experiment, all equipment and connecting lines, including the manifold and the lines leading to the mixing tank, are evacuated separately using the vacuum pump. Additionally, the shock tube was evacuated down to 425 Pa before the filling process. These steps are crucial for maintaining the integrity of the experiment and creating a controlled environment to obtain accurate results.

After filling the shock tube up to atmospheric pressure with the test gas, the solid aluminum plate that was initially installed on the end of the shock tube opposite the ignition wire for the vacuuming and filling processes is removed by a pneumatic system to open the tube to the ambient environment. This configuration is adopted to prevent any pressure waves reflected from the closed end and inducing the flame front.

As shown in Figure 2.1 an obstacle with a height of 51 mm is placed downstream of the flame front to investigate the flame vortical structure entrainment. The blockage ratio is 50 percent, and the obstacle is located at L_{Obc}= 159 mm. The distance is adopted based on Gharib et al. [4] work in introducing the L/D (stroke ratio) as a universal time scale for vortex ring formation (see Figure 2.2), where L is the piston stroke and D is the diameter. Their results indicate that the flow field generated by large enough L/D consists of a leading vortex ring followed by a trailing jet. The vorticity field generated by small stroke ratios shows only a single vortex ring of the leading vortex and is disconnected from that of the trailing jet. The transition between these two distinct states is observed to occur at a stroke ratio of approximately 4. In all cases, the maximum circulation that a vortex ring can attain during its formation is reached at this non-dimensional time or formation number which is in the range of 3.6 to 4.5 for a broad range of flow conditions.

In the second set of experiments for visualizing the third dimension of the flame, as we installed two rectangular mirror prisms in top and bottom walls, to have the same L/D as in the first set of experiments, we adopted an obstacle with a height of 32 mm and L_{Obc}= 100 mm.

2.2 Visualization

Flame propagation and flow field ahead of flame are visualized by using Edgerton shadowgraph [5, 22] and Schlieren [22] techniques. These two methods translate density gradients of transparent media such as air, water, and glass into regions of light and dark. The high-speed camera, Phantom v1210 used has a resolution of 1024 pixels by 288 pixels at 41420 frames per second for an interframe time of approximately 24.14 micro-seconds.

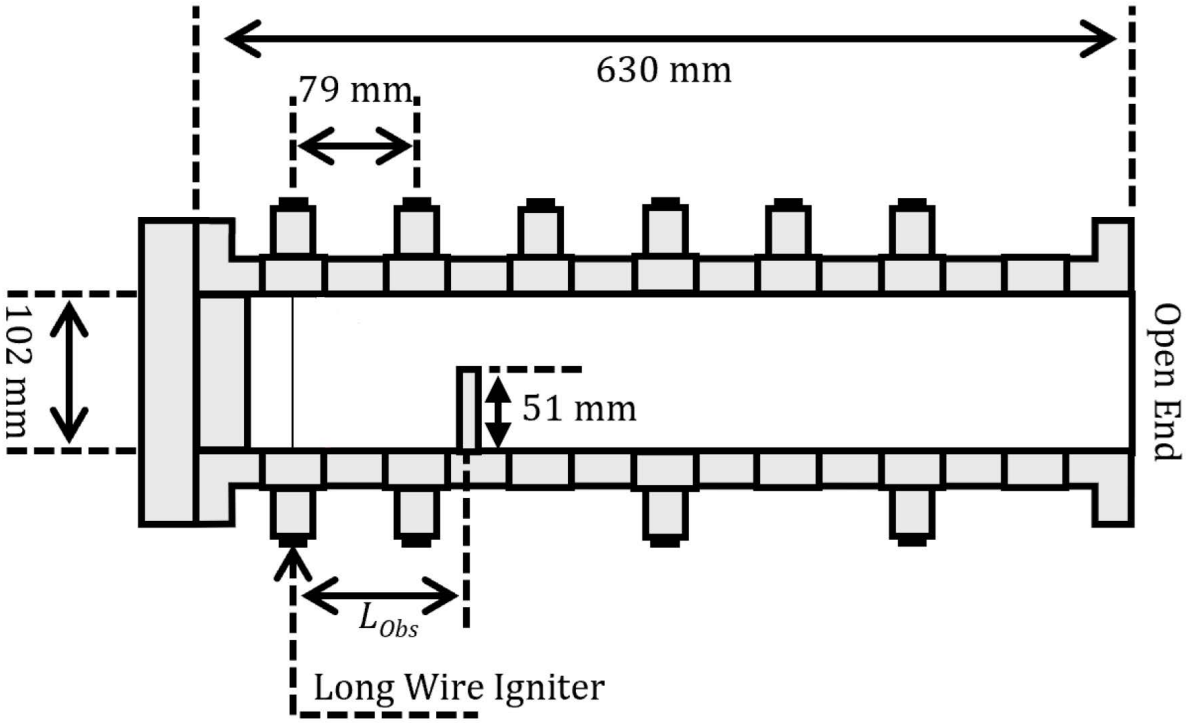

Figure 2.1: Diagrams of the experimental setup and shock tube configuration

2.2.1 The Edgerton Shadowgraph technique

The shadowgraph technique relies on the refraction of light rays passing through a medium with varying density. When a beam of light travels through a region where the refractive index changes, the light rays are bent. These bends cause variations in the intensity of light projected onto a screen or captured by a camera, resulting in a visual representation of the density gradients within the medium.

A 1000 W arc lamp is used as a collimated light source to produce a parallel beam of light. This ensures that the light rays are straight and uniform before passing through the test section. The collimated light exiting from the arc lamp is condensed to a 3-5 mm point using a 50 mm glass lens. To avoid any blurriness in the image, the light source should be small.

A retroreflective screen was used in the shadowgraph visualization setup. It was positioned opposite the light source, allowing visual access to the experiments. Retroreflective materials have the unique property of reflecting light back with minimal scattering. This screen

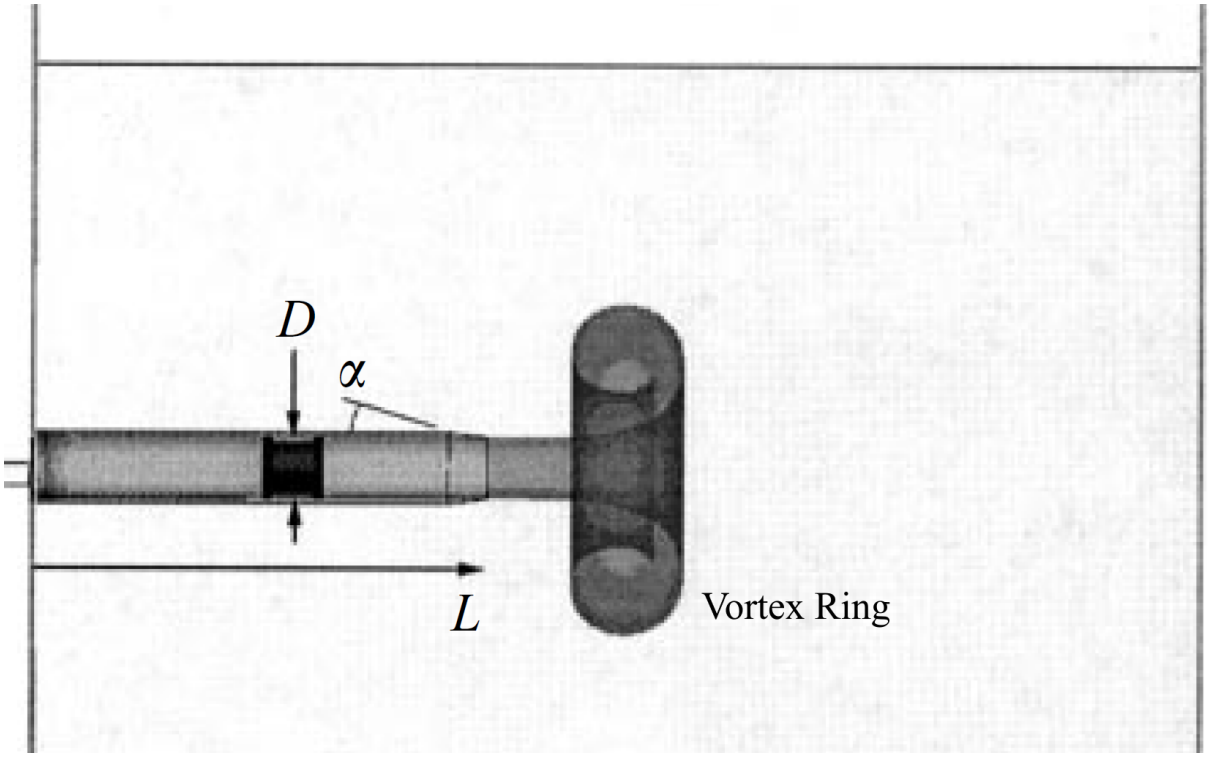

Figure 2.2: General schematic of piston stroke in formation of vortex ring [4]

reflects light rays back towards their source, the parallel light rays are then refocused by a second lens or mirror. The high-speed camera is placed near the light source to capture the reflected light. The camera records the shadowgraph images, which show the density variations within the test section Figure 2.3. If the second derivative of density is not constant, the region where this occurs will appear dark, or as a shadow.

2.2.2 The Z-type Schlieren technique

Schlieren photography relies on the fact that light rays are bent whenever they encounter changes in the density of a fluid. In the Schlieren Z-Type method, two concave mirrors on either side of the test section are assembled. The arc lamp placed opposite the camera is used as the source of light. The light beams pass through a slit that is placed in front of the arc lamp to create parallel rays passing through the test section. On the other side, the parallel rays are collected by the second mirror, converging to a focal point at the knife edge, and then the rays continue to the camera lens.

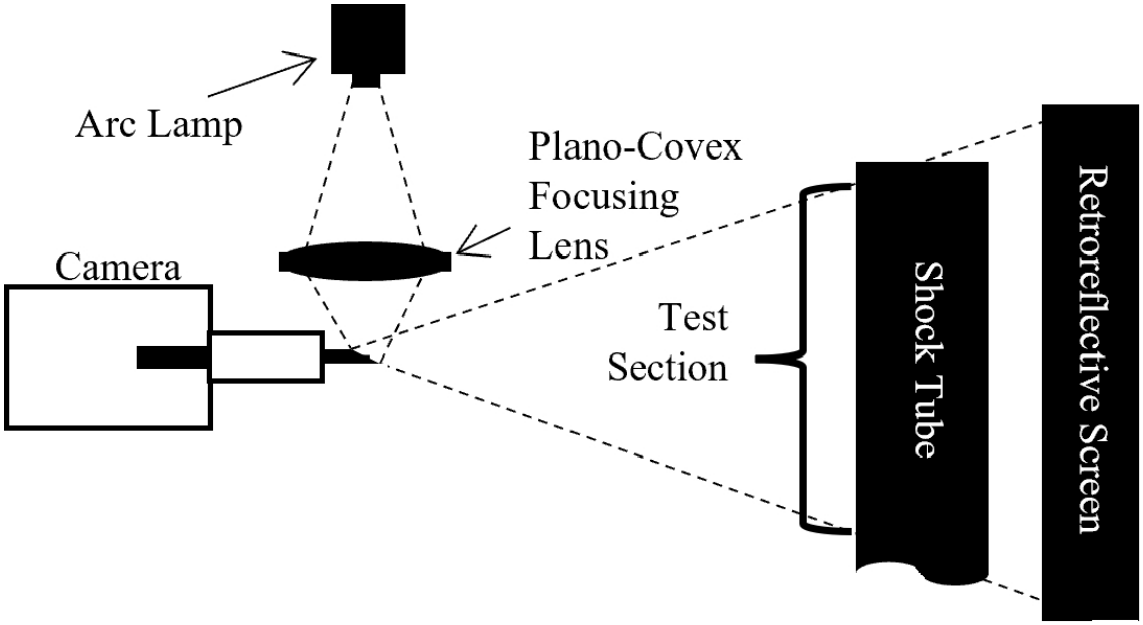

Figure 2.3: Shadowgraph technique arrangement

Inside a medium with a non-constant first derivative of the density field, the refractive index changes. These variations cause light rays to bend or deviate from their original path as they pass through the medium. The light rays are focused onto the knife-edge after passing through the test region. The knife-edge blocks part of the refracted light, creating areas of light and shadow that correspond to density changes.

If light rays are deflected towards the knife-edge, the part of the image where those light rays originate from will be darkened more than a part of the image with constant density (these rays do not pass through the focal point and are stopped by the knife-edge). Conversely, if light rays are deflected away from the knife-edge, that part of the image will appear brighter than unaffected regions of the image. Thus, Schlieren setups are only sensitive to density gradients normal to the knife-edge, while shadowgraph visualization is uniformly sensitive in all directions.

2.2.3 Three-dimensional visualization setup

A novel technique was developed to visualize the flame in three dimensions. In this method, two parallel prism mirrors were installed on the top and bottom walls of the shock tube.

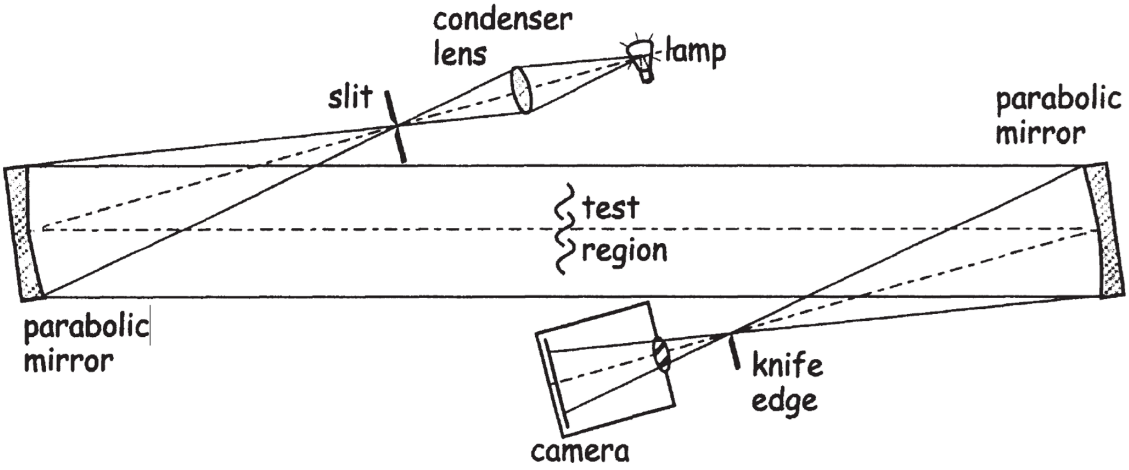

Figure 2.4: Z-type Schlieren arrangement [5]

The prism mirrors used in the experiments were custom fabricated by Canus Plastics, located in Ottawa. Each piece consists of a triangular prism made from acrylic, with an acrylic mirror pane mounted above it. The two base sides of the prism mirrors are 19 mm in length, and their longitudinal length is 447 mm, as shown in Figures 2.5 and 2.6.

The most important specifications for these two components were the optical quality of the mirrors, to ensure a clear and undistorted view, and the precise dimensions, which were necessary to achieve perfectly parallel mirror alignment when the prism mirrors were installed inside the shock tube.

The evolution of the flame as it propagated over the obstacle was visualized using the shadowgraph technique.

In this setup, the position of the camera relative to the shock tube, both in terms of distance and height, was important for obtaining accurate and undistorted images. Additionally, as the prism mirrors inside the shock tube acted as a periscope, maintaining their exact parallel orientation was essential to avoid any image misalignment.

In the first step, we needed to test the functionality of each mirror to ensure accurate visualization. We began by installing the first mirror on the bottom wall of the shock tube. To verify the mirror's alignment and reflective accuracy, we attached a readable note to the top wall of the shock tube Figure 2.7. This note worked as a reference point, to check whether the mirror displayed the width of the shock tube properly.

In the second step, we needed to ensure that the two mirrors were exactly parallel to examine the periscope functionality of the mirrors. To achieve this, we installed the second

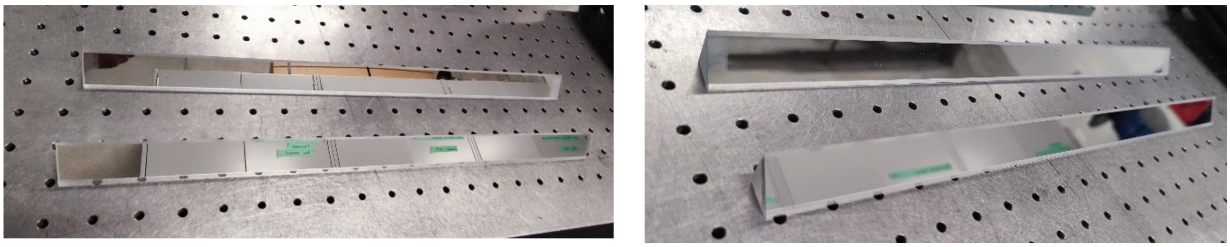

Figure 2.5: The prism mirrors for three-dimensional visualization

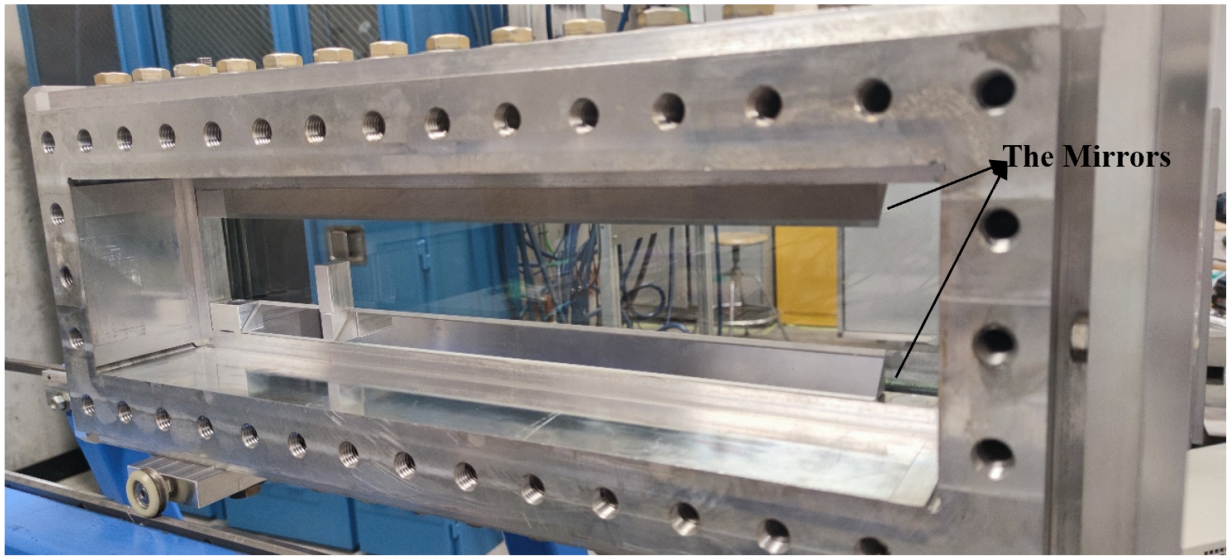

Figure 2.6: Mirrors configuration inside the shock tube for three-dimensional visualization

mirror on the top wall of the shock tube, then attached our note directly behind the second mirror on the shock tube glass Figure 2.8. By capturing several photos from the field of view of the bottom mirror, we were able to verify the alignment of the mirrors. This step was necessary to confirm that the mirrors functioned correctly as a periscope, allowing us to accurately observe the reflected images.

Figure 2.9 illustrates the path of light beams for three-dimensional visualization. Light emitted from the arc lamp traveled through the shock tube, initially reaching the bottom prism mirror. It then reflected off the top prism mirror, which redirected the light onto the retroreflective screen located directly behind the shock tube. At this point, the flame shape in the third dimension along the width of the shock tube appeared on the retroreflective screen. The light rays then retraced their exact path, returning from the screen to the

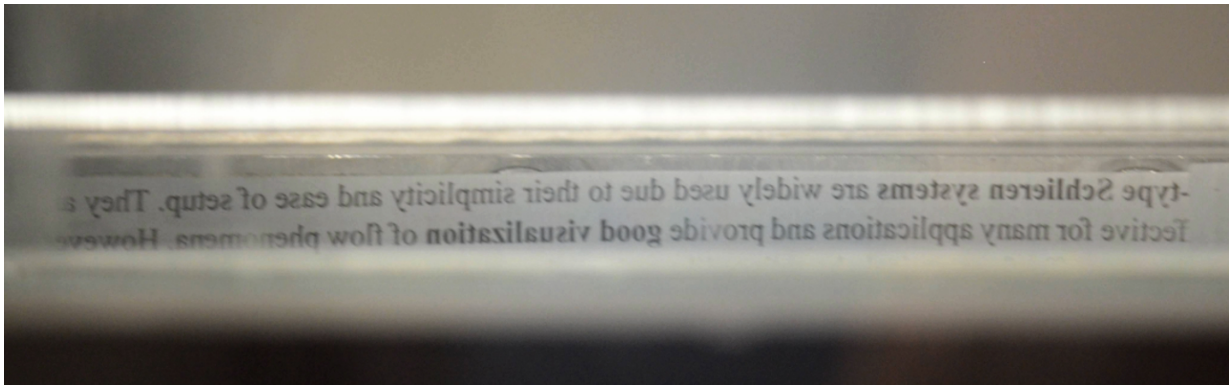

Figure 2.7: The bottom mirror's visualization of the shock tube's width

camera positioned in front of the shock tube to capture the flame's three-dimensional picture (In this scheme, the light path for the third dimension visualization was just drawn).

2.2.4 Test Gases

As mentioned earlier, the experiments were carried out for three mixtures: stoichiometric methane-air, stoichiometric hydrogen-air, and a stoichiometric equimolar blend of methane and hydrogen with air. For both sets of experiments, we used the same combustible mixtures.

The partial pressure method was used for preparing the detonable gaseous mixtures. The pipelines and the mixing tanks were initially evacuated to a pressure of 40 Pa. This is important to remove any residual air or contaminants from the tank, to ensure the gas mixture composition and the quality of the flames, and to have reliable mixtures. Firstly, the combustible fuel was added to the mixing tank until its calculated partial pressure value, as shown in Table 2.1. The inert diluent was added after the fuel gas, if applicable, and finally, the oxidizer was added based on its partial pressure. For mixing and homogenization of the gases, the mixture was allowed to remain for one day before starting the experiments.

As an example of preparing a mixture in the experiments, for the stoichiometric hydrogen-air mixture, the mixing tank pressure was raised to 33.8 psi. Initially the tank was filled with hydrogen to 10 psi, and then nitrogen was added until the pressure gauge showed 28.8 psi, and finally, oxygen was added up to 33.8 psi.

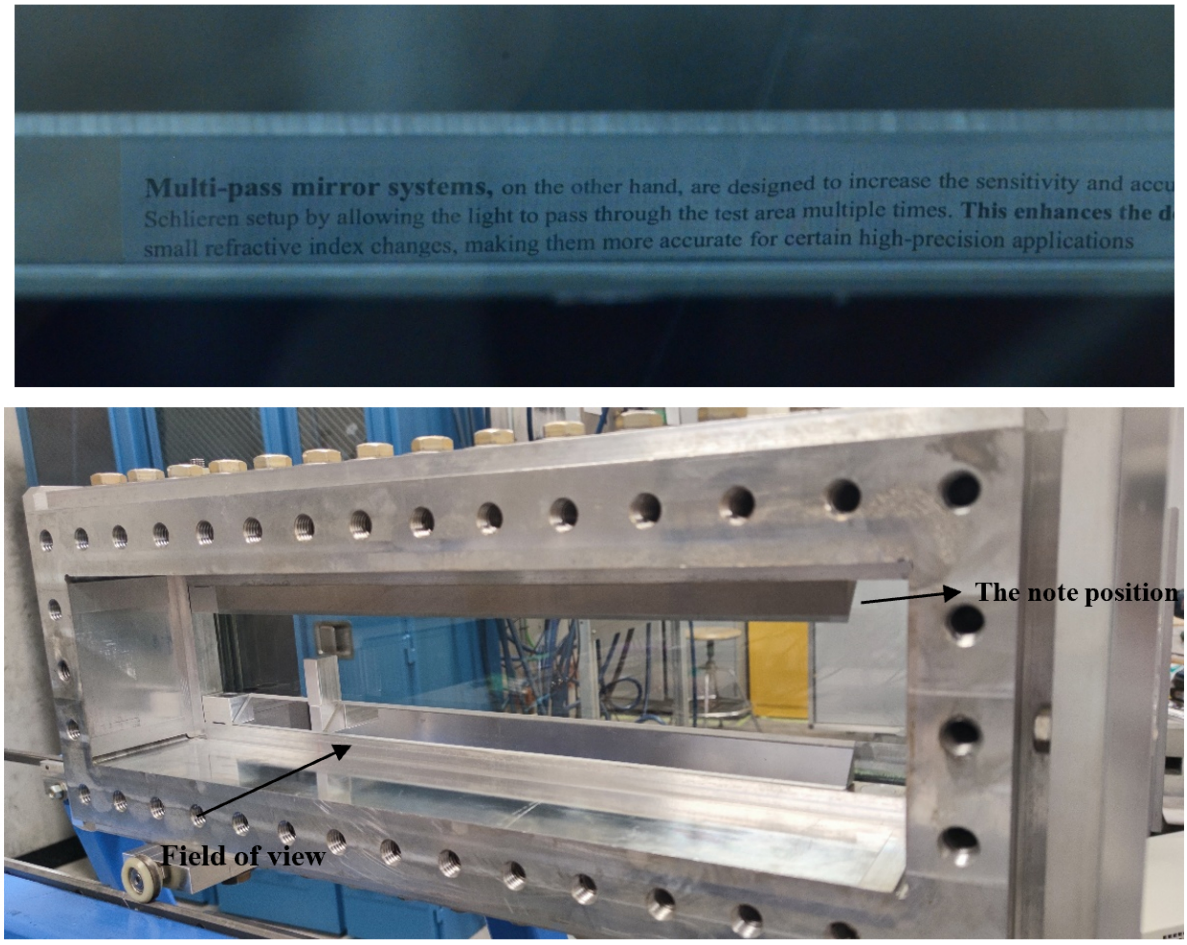

Figure 2.8: Checking the mirrors periscope functionality

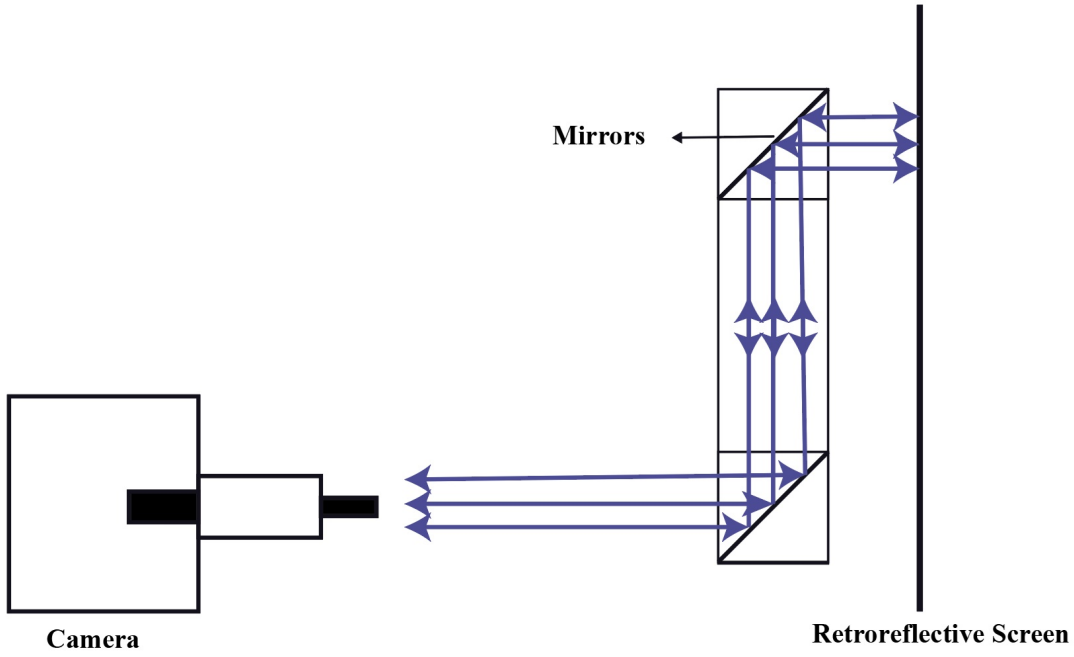

Figure 2.9: Schematic path of light beams

Table 2.1: Composition of test gases for the experiments

$2H_2 + O_2 + 3.76N_2$			
H_2(psi)	N_2(psi)	O_2(psi)	Tank Pressure (psi)
10			10
	10/2×3.76=18.8		28.8
		5	33.8
$CH_4 + 2O_2 + 7.52N_2$			
CH_4(psi)	N_2(psi)	O_2(psi)	Tank Pressure (psi)
3			3
	22.6		25.6
		6	31.6
$CH_4 + H_2 + 2.5O_2 + 9.4N_2$			
CH_4(psi)	H_2(psi)	N_2(psi)	O_2(psi)	Tank Pressure (psi)
3				3
	3			6
		28.2		34.2
			7.5	41.7

Chapter 3

Flame Vortex Entrainment

The evolution of the flame as it passes over the obstacle was visualized using Schlieren and shadowgraph photography to capture the flame front details and the flow field downstream of the flame. The vortex, trailing jet, and recirculation zone behind the obstacle were visualized using the Z-Type 2-Mirror Schlieren System. Additionally, to visualize the flame front structure and propagation alongside the shock tube over longer distances, the shadowgraph technique was used. In this chapter, the experimental data for flame evolution and entrainment in vortical structures are presented for the following mixtures: stoichiometric hydrogen-air, stoichiometric methane-air, and stoichiometric equimolar blend of these two fuels with air.

3.1 Hydrogen-Air mixture

Selected frames in Figure 3.1 represent the flame evolution in a stochiometric hydrogen-air mixture. A cellular flame was ignited by the tungsten wire installed near the end of the channel, and the flame started propagating toward the other end of the shock tube. A rectangular obstacle with a 50 percent blockage ratio was located downstream of the flame. As the flame ignited and propagated, the high expansion ratio (σ) between the burned and unburned sides caused the burned gas to expand and drive a flow downstream. Consequently, the pressure inside the shock tube started increasing. Pressure waves were generated during the build-up and propagation of the flame and propagating ahead of the flame [6]. With the presence of the obstacle and due to Kelvin-Helmholtz instability, a turbulent shear layer and vortical structures were formed at the edge and behind the obstacle. The flame front, due to the stagnation point behind the obstacle and the flow

field over the obstacle, was stretched along the shock tube (2.4 ms frame to 2.89 ms frame). As the flame tip approached the shear layer and vortical structure behind the obstacle,it started wrinkling and being entrained into vortices. The rolling up of the flame in the vortical structure resulted in a considerable increase in the flame front surface area. The hydrogen flame was less prone to getting entrained into smaller-scale vortices (in the vortical structure behind the obstacle), which was observed for methane and equimolar flames, as discussed in the following two sections.

3.2 Equimolar Methane/Hydrogen-Air mixture

Figure 3.2 represents the flame evolution and propagation in an equimolar blend of hydrogen/methane with air. As the flame ignited and propagated, the flame front started to create initial cellular structures. In the 5.42 ms, 5.85 ms, and 6.25 ms frames, the formation of finger flames and the cusp regions are shown. Like hydrogen, when this flame reached the obstacle, leading to the acceleration of unburned gas flow in vena contracta, the flame stretched along the shock tube (6.25 ms frame). The flame front became wrinkled as it was entrained into the vortical structure. The equimolar flame interacted differently with the vortical structure compared to the hydrogen flame; the vortices broke the flame structure, disturbed the flame and we can see the equimolar flame had this propensity to roll up into smaller-scale vortices, which is observed in the 7.43 ms frame. Compared to the smooth flame front in the hydrogen mixture, the equimolar flame exhibited more texture in the flame front after getting entrained into the vortical structure.

3.3 Methane-Air mixture

Figure 3.3 represents methane-air flame propagation and entrainment in vortices. The flame ignited and started to propagate toward the open end. We can observe the formation of finger flames and a long cusp region, similar to that of an equimolar mixture. As the flame reached the obstacle, due to the acceleration of flame-driven flow above the obstacle, the flame front stretched along the shock tube in the 15.28 ms, 16.03 ms, and 16.62 ms frames. Then the flame got entrained into the turbulent shear layer and vortex behind the obstacle, and we can see the flame front wrinkled and rolled up into different scales of vortices (17.1 ms, 17.73 ms, and 18.28 ms frames).

The methane-air flame, like the equimolar blend, interacted differently with the vortical structure compared to the hydrogen flame; the vortices broke the flame structure and

disturbed the flame (17.1 ms, 17.73 ms, 18.28 ms and 19.03 ms frames).

In all three mixtures, during the flame rolling-up period within vortical structures, the flame front surface area increased considerably, leading to flame acceleration. This phenomenon will be discussed in the following sections, where the velocity and pressure diagrams are presented.

Selected frames in Figure 3.4 represent the evolution of the flames in the three mixtures. By propagating the flames inside the channel and the volumetric expansion of the burned gas, flame-induced flow was created ahead of the flames. With the presence of an obstacle downstream, a pressure gradient was generated, resulting in flames deformation and stretch as they approached the obstacle. Shortly thereafter, the flames were entrained into a vortical structure, which was the result of the flame-driven flow over the obstacle since the ignition of the flame and Kelvin-Helmholtz instability.

As a result of flame entrainment, the flame front surface area grew considerably. This growth led to an increase in the flame burning rate and total energy release rate in the channel. The more rapid combustion generated a stronger flow and accelerated the flame. As the flame area and fuel consumption rate increased, a strong compression wave propagated downstream, contributing to additional flame acceleration.

These three flames interacted differently with vortical structures. The hydrogen-air flame, as a reactive fuel, consumed the vortex rapidly as it rolled up into it. The flame was less prone to be disturbed by the vortex and the turbulent shear layer above the obstacle. In contrast, vortices disturbed and broke the flame structure in methane and equimolar mixtures, causing these flames to get entrained into them for a longer period. Additionally, in methane and equimolar flames, we observed the formation of pockets of unburned gas due to inefficiencies in the combustion process and local quenching associated with the flame front deformation and stretching.

Figure 3.5 illustrates the start of the vortex as the flame propagated and the flow field developed ahead of the flame. This figure captures the start and growth of the vortex in the hydrogen and equimolar blend mixtures. Schlieren photography was employed to capture the turbulent shear layer and vortical structures due to its higher sensitivity to density gradients in the flow field compared to shadowgraph techniques. Hydrogen, with its higher flame speed, generated a stronger downstream flow field with greater density gradients. This is why the field in Figure 3.5 appears clearer for hydrogen compared to the equimolar blend. As the flame speed in the methane-air mixture is lower than in the other two, the vortex became less visible in the Schlieren images and was excluded from this figure.

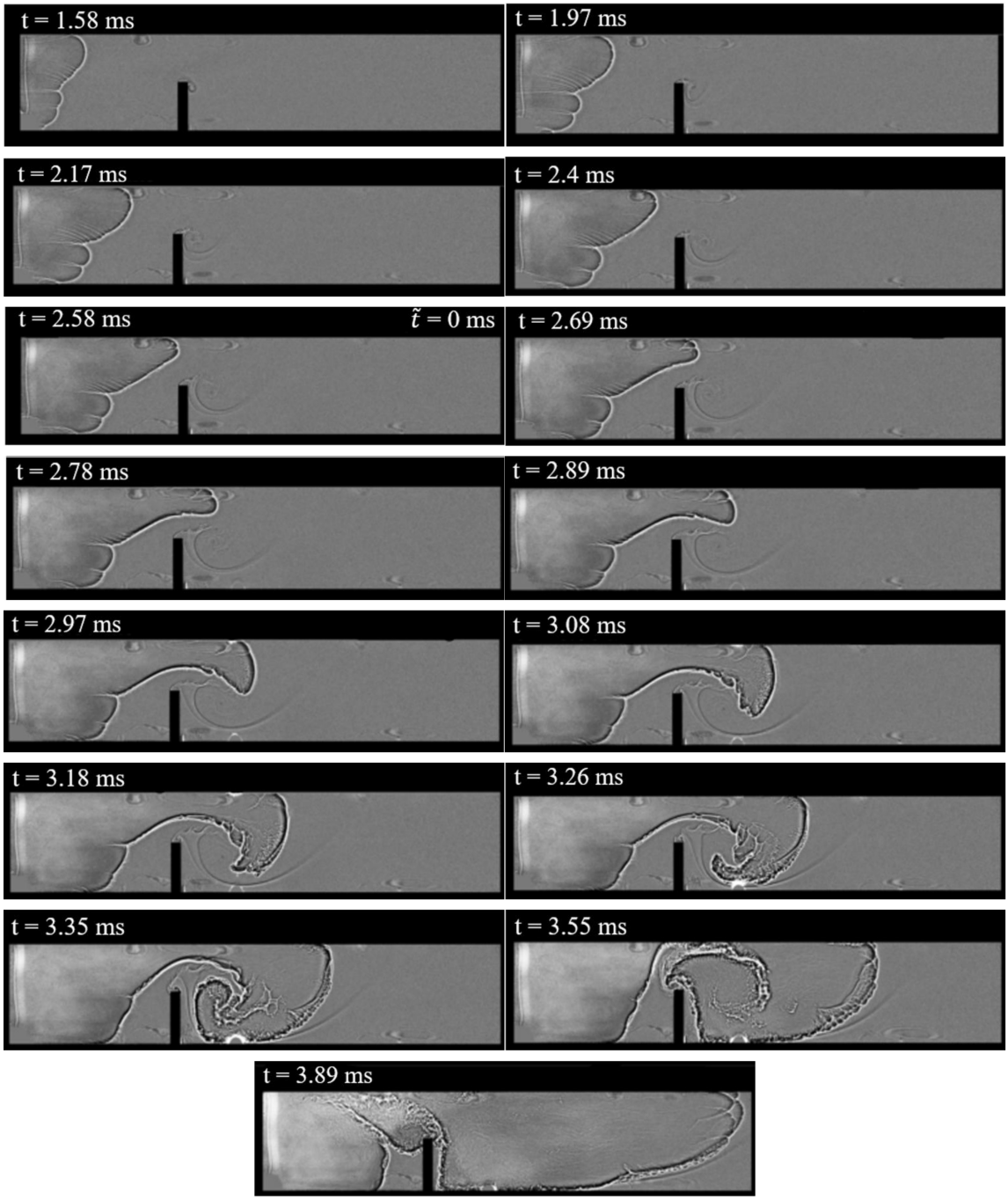

Figure 3.1: Evolution of the stochiometric hydrogen-air flame visualized using shadowgraph technique. Times are shown above each frame and t=0 is the time when the flame ignites and $\tilde{t} = 0$ is the moment the flame tip crosses the leading edge of the obstacle.

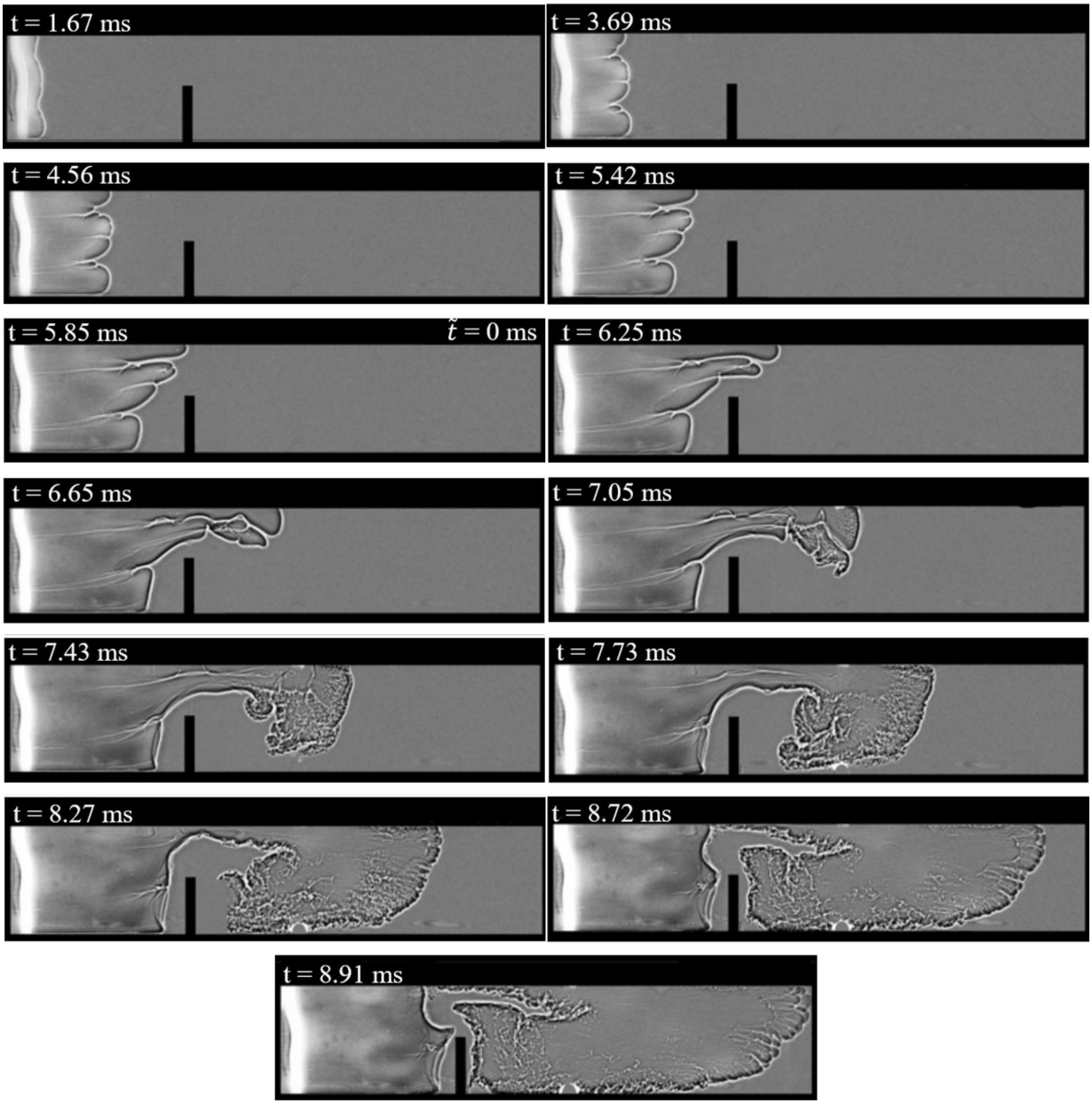

Figure 3.2: Evolution of the equimolar flame visualized using shadowgraph technique. Times are shown above each frame and t=0 is the time when the flame ignites and $\tilde{t} = 0$ is the moment the flame tip crosses the leading edge of the obstacle.

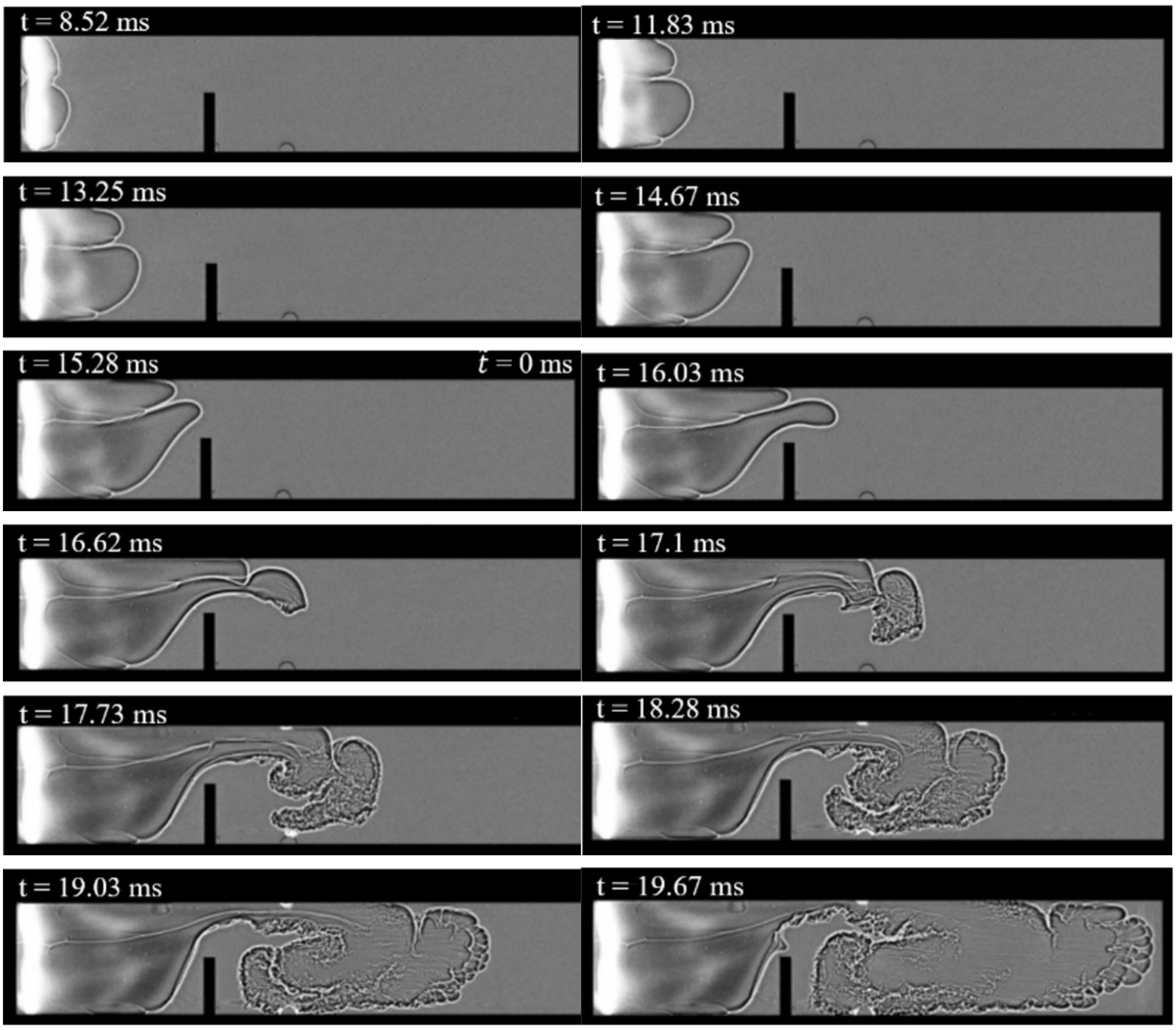

Figure 3.3: Evolution of the methane-air flame visualized using shadowgraph technique. Times are shown above each frame and t=0 is the time when the flame ignites and $t = 0$ is the moment the flame tip crosses the leading edge of the obstacle.

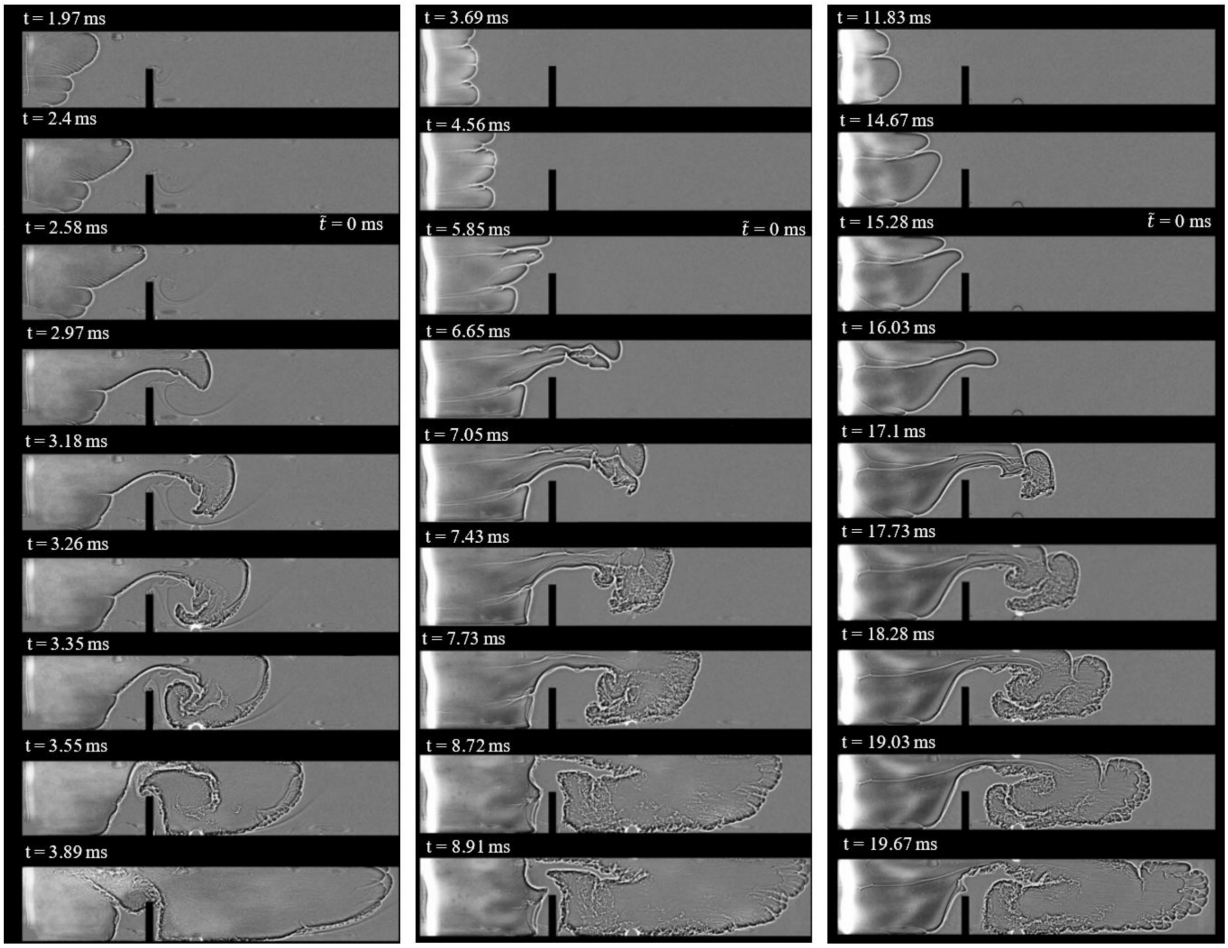

Figure 3.4: Evolution of the flames in the three mixtures visualized using shadowgraph technique. Times are shown above each frame and t=0 is the time when the flame ignites and $\tilde{t} = 0$ is the moment the flame tip crosses the leading edge of the obstacle.

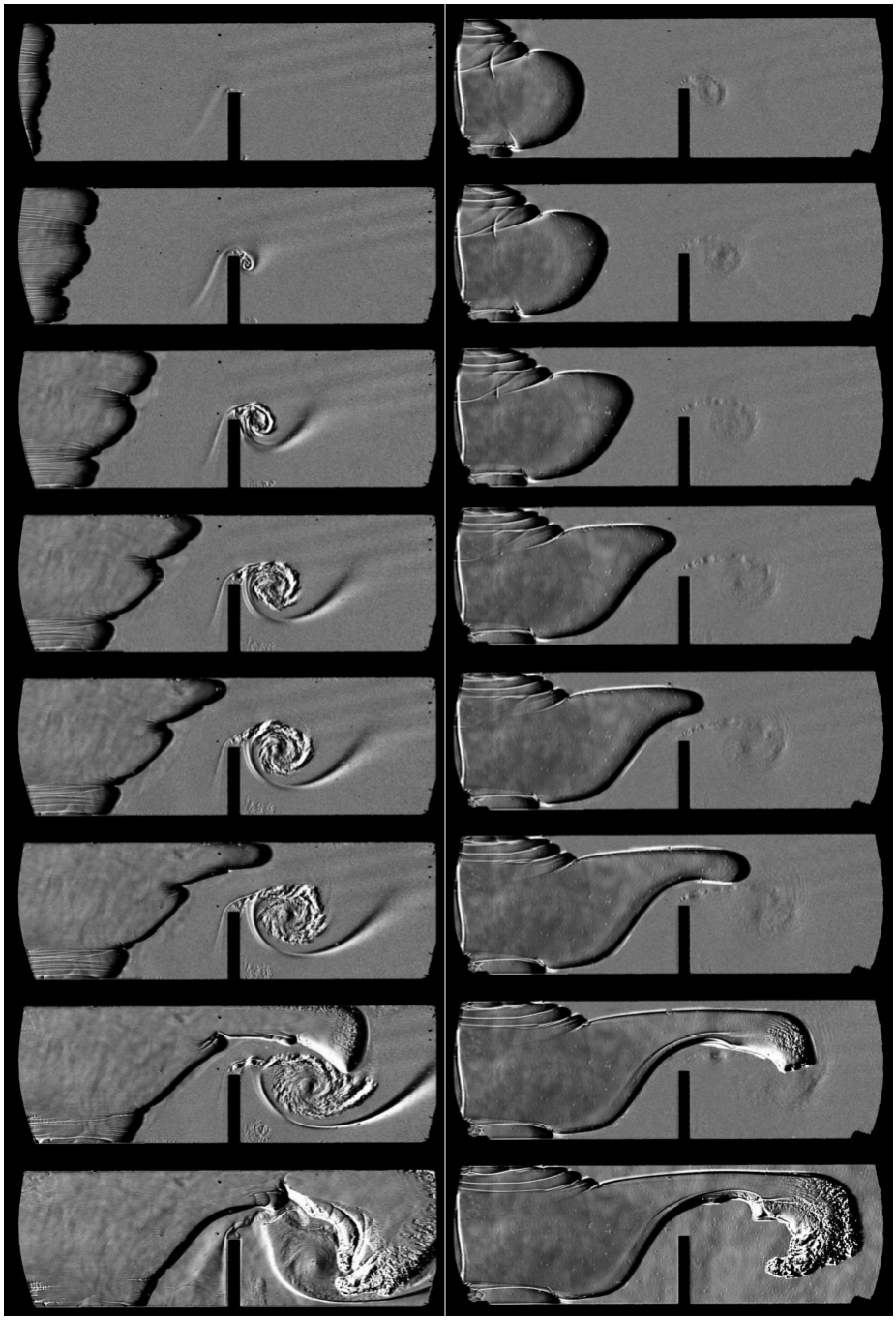

Figure 3.5: Evolution of the vortical structure and flame, visualized using Schlieren in hydrogen (left side) and equimolar (right side) mixtures.

Figures 3.6, 3.7, and 3.8 illustrate the evolution of the flame tip velocity over time. The velocity was measured as the forwardmost flame front location along the horizontal axis in experimental photographs. To assess repeatability, more than ten experiments were carried out for each mixture. Each curve has been adjusted in time such that the flame tip crosses the leading edge of the obstacle at $t = 0$. It was evident that the hydrogen flame propagated significantly faster than the methane flame, while the equimolar blend propagated at a speed in-between the two extremes throughout the experiment. After the flames rolled up into vortical structures and accelerated, but before they exited the field of view, the highest recorded velocity was approximately 400 m/s for the hydrogen flame, and around 220 m/s and 135 m/s for the equimolar and methane flames, respectively.

The flame tip velocity evolved similarly in each mixture. Initially, there was a gradual increase in velocity for negative times, which was associated with the initial growth of cellular structures along the flame surface from a relatively flat ignition kernel due to the effects of boundary layer and Landau–Darrieus instabilities. Shortly before time zero, a much sharper increase was observed related to natural contraction and acceleration of downstream flow ahead of the obstacle in vena contracta.

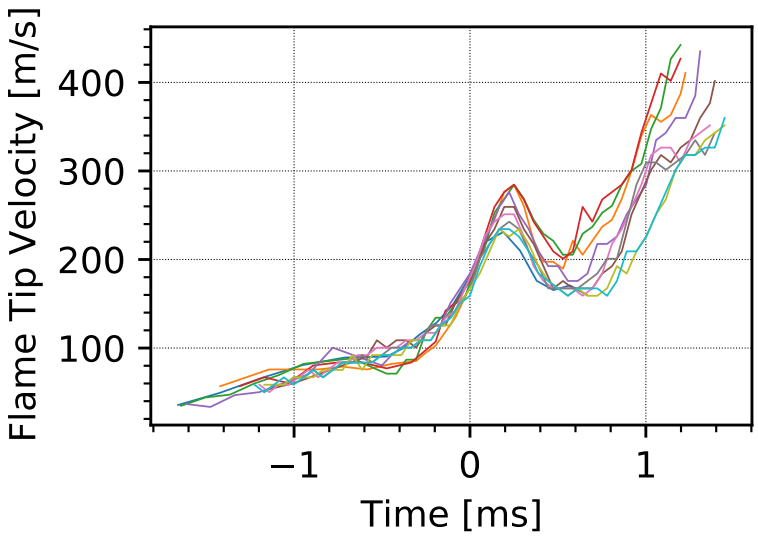

Figure 3.6: Evolution of the flame tip velocity for hydrogen-air flame over time. Time $t = 0$ is defined as the moment when the flame tip crosses the leading edge of the obstacle.

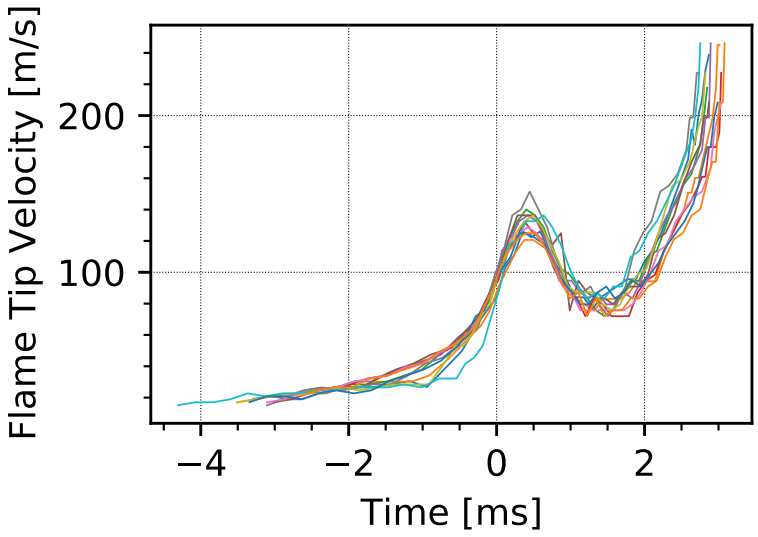

Figure 3.7: Evolution of the flame tip velocity for equimolar blend-air flame over time. Time $t = 0$ is defined as the moment when the flame tip crosses the leading edge of the obstacle.

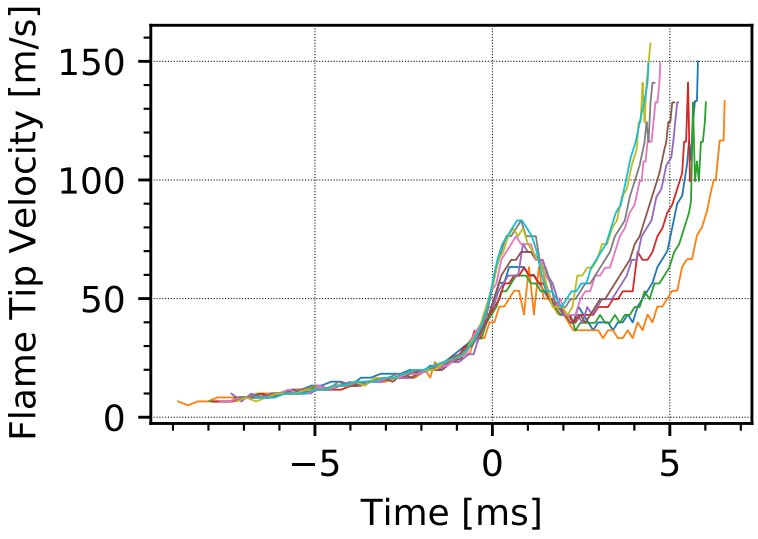

Figure 3.8: Evolution of the flame tip velocity for methane-air flame over time. Time $t = 0$ is defined as the moment when the flame tip crosses the leading edge of the obstacle.

This increase in flame tip velocity was the result of the flame's deformation in the vicinity of the obstacle. The deformation was caused by the Rayleigh-Taylor mechanism induced by flow gradients that occurred due to the acceleration of the flow through the vena contracta and the misalignment of the pressure gradient in the flow field and the density gradient across the flame sheet. The velocity field of the flow ahead of the flame dictated both the propagation and deformation of the flame. When the flames passed through the vena contracta, there was a sudden enlargement in cross-sectional area that caused flow divergence. Due to this flow divergence and flame entrainment in vortices, flame tip velocity decreased for a short period. This decrease in flame speed continued until a minimum was reached. At this point, there was a reactive coupling between the increase in burning rate associated with the enhancement in flame surface area resulting from the flame roll-up, and the strong acceleration of flow induced ahead of the flame by the rapid expansion of the burned gases. This acceleration of the flame tip continued until the flame exited the field of view.

As mentioned, to assess repeatability, around ten experiments were carried out for each mixture. There was some discrepancy between the data in the aforementioned figures, specifically in the last part showing flame acceleration after roll-up in the vortical structure. As the formation of a shear layer at the leading edge of the obstacle and the eddies behind it is a turbulent phenomenon that could vary across the experiments, the flame deformation and entrainment into the vortical structure were not exactly the same in each experiment.

The evolution of the pressure inside the shock tube is presented in Figures 3.9, 3.10, and 3.11 where the pressure is plotted against time. The hydrogen flame exhibited the highest overpressure peak, reaching up to 100 kPa, while the methane flame generated the weakest overpressure, with a 15 kPa peak. The overpressure peak for the equimolar blend was around 60 kPa inside the shock tube. There was an initial increase in pressure associated with the initial increase in the cellular structure of the flames. When the flames reached the vena contracta, due to sudden depressurization in the throttle, there was a pressure decay for a short period. The maximum pressure peak inside the shock tube was recorded as the flames rolled up into the vortical structures and enhancing the burning rate of the fresh gases.

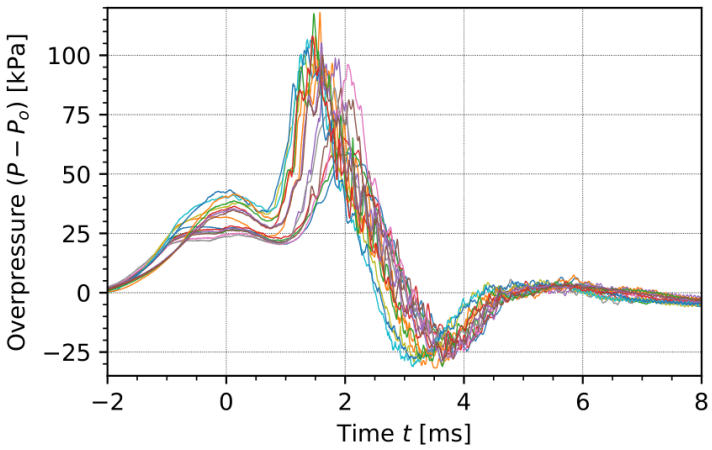

Figure 3.9: Evolution of the pressure inside the shock tube for hydrogen-air flame over time. Time $t = 0$ is defined as the moment when the flame tip crosses the leading edge of the obstacle.

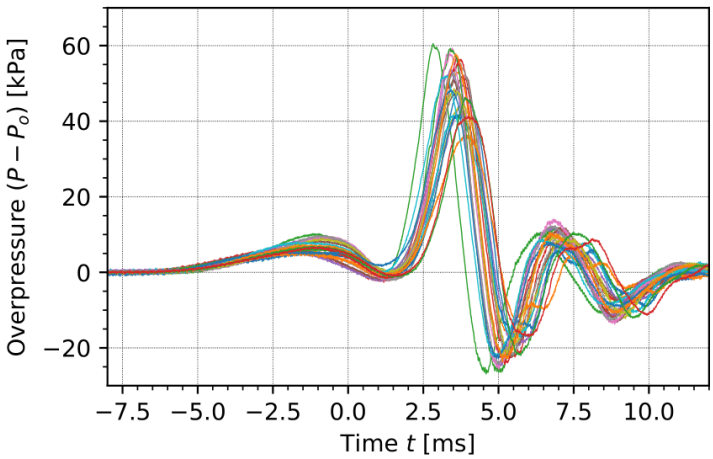

Figure 3.10: Evolution of the pressure inside the shock tube for equimolar blend-air flame over time. Time $t = 0$ is defined as the moment when the flame tip crosses the leading edge of the obstacle.

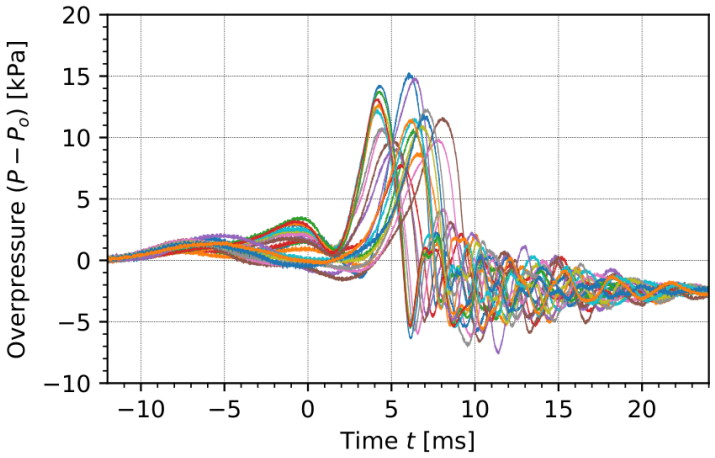

Figure 3.11: Evolution of the pressure inside the shock tube for methane-air flame over time. Time $t = 0$ is defined as the moment when the flame tip crosses the leading edge of the obstacle.

In the presence of an obstacle downstream of the flame, the flame-driven flow created a multiscale turbulent shear layer at the leading edge of the obstacle and the large eddy behind it. As the flame was entrained into vortices, pockets of unburned gases were created due to inefficiencies in the combustion process and local quenching associated with the flame front deformation and stretching. In the hydrogen-air mixture, these pockets combusted at a faster rate as a result of the mixture's higher reactivity compared to other mixtures. Consequently, a substantial amount of gas was burned within the hydrogen flame over a shorter period, leading to a higher peak pressure.

Following the sudden acceleration of the flame after vortex entrainment, an expansion wave propagated in the opposite direction on the burned gas side, leading to a pressure drop in the shock tube. After the pressure peak and its subsequent decay, both resulting from the flame-vortex interaction, a smaller pressure peak was observed, which is more noticeable in the methane and equimolar blend mixtures. This secondary peak was associated with the combustion of gases exiting the shock tube as the flame was entrained into the vortical structures.

3.4 Characteristic scales for data reduction

As mentioned, these three flames interacted differently with the vortical structures, which can be attributed to variations in their flame properties. Characteristics such as laminar burning velocity differ by an order of magnitude, as shown in Table 3.1. Therefore, to better understand flame behavior and its interaction with flame-driven flow, we express the pressure and velocity measurements from the experiments in a non-dimensional form. This approach effectively eliminates the influence of the distinct flame laminar velocity of each mixture. In this way, the scaled data reflect only the flame's response to the dynamics of the flow field. In the following section, we define appropriate scaling factors to normalize the experimental velocity and pressure data.

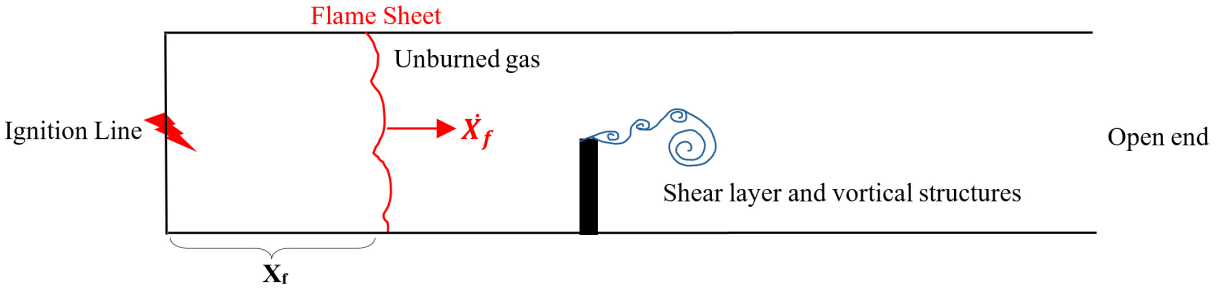

Figure 3.12: Flame-driven flow creates a multiscale turbulent structure in the presence of an obstacle downstream.

The conservation of mass across the flame sheet, in the flame's frame of reference, can be written as:

$$\rho_u \left(\dot{X}_f - u \right) = \rho_b \left(\dot{X}_f - u_w \right) \tag{3.1}$$

Where u is the velocity of the flame-driven flow and u_w is the velocity of burned gas, which is equal to zero due to the closed end in the ignition line. S_L is the laminar burning velocity of flame.

By considering:

$$\dot{X}_f - u = S_L \tag{3.2}$$

and

Table 3.1: Mixtures composition and flame properties at atmospheric conditions (P= 101.2 kPa, T= 295 K).

Set	Properties	$2H_2 + O_2 + 3.76N_2$	$CH_4 + H_2 + 2.5O_2 + 9.4N_2$	$CH_4 + 2O_2 + 7.52N_2$
1	Flame thickness δ_f (mm)	0.34	0.36	0.48
2	Laminar flame speed S_L(m/s)	2.21	0.55	0.34
3	Flame time δ_f/S_L (ms)	0.154	0.654	1.41
4	Expansion ratio(σ)	6.93	7.44	7.61
5	Unburned gas density(kg/m^3)	0.86	1.07	1.14
6	Damköhler number*	2.4	0.93	0.61

*See section 3.6

$$\frac{\rho_u}{\rho_b} = \sigma \tag{3.3}$$

σ is expansion ratio across the flame sheet.

From (3.1), (3.2), and (3.3):

$$\dot{X}_f = \sigma S_L \tag{3.4}$$

$$u = (\sigma - 1) S_L \tag{3.5}$$

The flame tip velocity was normalized by the factor σS_L, and the overpressure inside the tube was scaled by the dynamic pressure $\rho_u \sigma^2 S_L^2$.

A characteristic time is the time taken for a laminar flame to travel the distance between the ignition line and the obstacle (L_{obs}). It is defined as:

$$t_{\text{dyn}} = \frac{L_{\text{obs}}}{\sigma S_L} \tag{3.6}$$

3.5 Experimental Scaling

The overpressure inside the tube was scaled by the dynamic pressure $\rho_u \sigma^2 S_L^2$, and the flame tip velocity was normalized by the factor σS_L. Figure 3.13 illustrates the non-dimensionalized flame tip velocity over a time non-dimensionalized by the dynamic time. It is important to note that the moment when the flame tip crosses the leading edge of the obstacle is represented by $t = 0$. The equimolar blend mixture had the highest scaled velocity, followed by the methane mixture. The hydrogen mixture exhibited the lowest scaled velocity.

In terms of normalized flame tip velocity, the three mixture diagrams overlapped and agreed at early times. This is because, immediately after ignition, the flames were nearly planar in form and had not yet been influenced by the downstream flow field. As the flames advanced through the shock tube and approached the obstacle, the flow dynamics ahead of them induced the formation of cellular structures and wrinkling, and the flames exhibited different behaviors (see Figure 3.4).

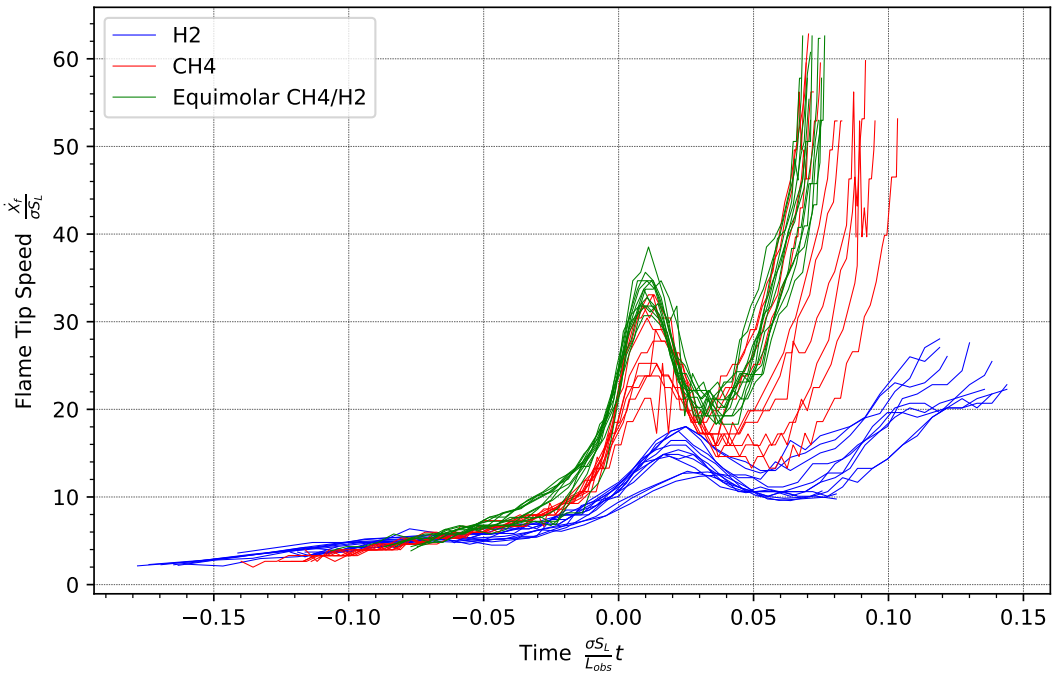

Figure 3.13: Scaled flame tip velocity as a function of scaled time.The time flame tip crosses the leading edge of the obstacle is represented by $t = 0$.

These three flames responded differently to the flow dynamics, which is the main reason for the differences between the unscaled and scaled data. The acceleration of the flame resulted from the increase in surface area and, consequently, the burning rate. The hydrogen flame propagated noticeably slower than the other two in the scaled form because it rapidly consumed vortices when rolled up into them and was less prone to wrinkling and involvement in smaller-scale vortices. In contrast, the dynamics of the downstream flow and vortices disrupted the methane and equimolar flames, breaking their structure and causing additional wrinkling and surface area enhancement along the flame front.

Figure 3.14 illustrates the non-dimensionalized overpressure inside the shock tube over a time non-dimensionalized by the dynamic time. Despite the higher overpressure peak for the hydrogen mixture (refer to Figure 3.9), the normalized overpressure of both the equimolar blend and methane-air flames was much higher than that of hydrogen-air flames. The maximum normalized pressure in the equimolar blend flame did not lie between the pressures of the two extreme mixtures. On the contrary, it was amplified to almost double the amplitude of the maximum scaled pressure in the methane-air mixture.

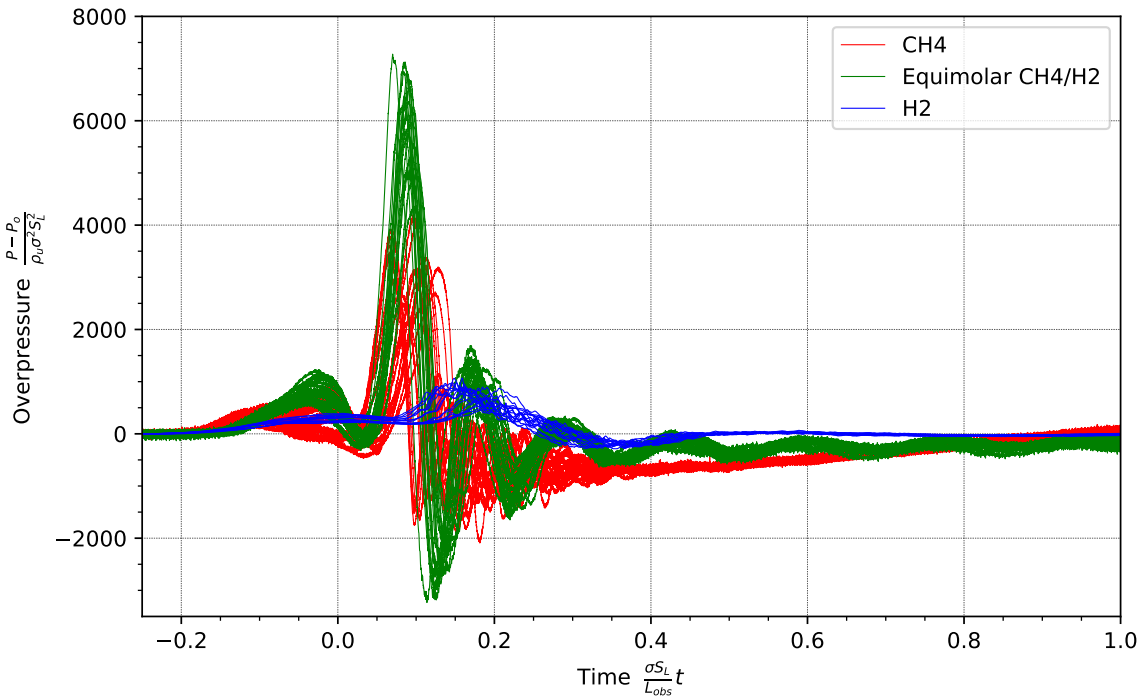

Figure 3.14: Scaled over pressure as a function of scaled time.The time flame tip crosses the leading edge of the obstacle is represented by $t = 0$.

When scaling the flame propagation velocity and pressure, it became apparent that the hydrogen flame had a smaller surface area enhancement compared to the methane and equimolar hydrogen-methane flames. In Table 3.1, the flame time was defined as the ratio of the flame thickness to the laminar burning velocity. It can be observed that hydrogen-air had a much shorter flame time compared to the other mixtures, allowing it to consume flame folds more quickly. This results in less surface area enhancement, as the smaller folds were used up faster than they could expand, and the increase in the flame front area was thus mainly due to the deformation of the larger scales of the flame surface. In the other mixtures, the efficient folding of the flame surface at smaller scales also contributed to their larger surface areas, as the consumption of these folds could not keep pace with their growth.

Additionally, to compare the scaled data of methane and equimolar mixtures, we can refer to Shi et al. work [14]. They studied the effects of differential diffusion of hydrogen on the flame structure in laminar premixed fuel-lean H_2/CH_4/air polyhedral flames. The results reveal that the positively curved troughs in the flame front, have significantly higher H_2 mole fraction compared to the negatively curved cusps, due to the respective focusing/defocusing effect of curvature on highly diffusive H_2. Consequently, the local equivalence ratio and temperature in trough regions are higher than those of cusps.

In our case study, as the flames rolled up into the vortical structures, they could locally quench due to flame front stretching. In the equimolar flame, the increased concentration of hydrogen in the positive curvatures of the flame front, compared to its planar form, reduced the extent of local quenching induced by turbulence. Due to the higher reactivity of hydrogen fuel, the equimolar flame could survive better than the methane flame from quenching and recorded a higher normalized overpressure.

3.6 Flame area amplification in the mixtures

These three flames interacted differently with the vortical structures, which can be explained by variations in their flame properties, such as flame time. The relation between the characteristic time of the flow field and the characteristic time of the flame (as presented in Table 3.1) appears to govern the flames' behavior in terms of vortex entrainment. To explain this behavior, we can refer to the definition of the Damköhler number, which represents the ratio of the characteristic time of the length scale vortex to the characteristic time of the flame, as defined by (3.7):

$$Da = \frac{t_L}{t_f} = \frac{\frac{d_L}{V_L}}{\frac{\delta_f}{S_L}} \tag{3.7}$$

Where d_{L} and V_{L} represent the diameter and tangential velocity of the large eddy. These were measured from the experimental photographs and presented in Table 3.2, δ_{f} and S_{L} are the flame properties listed in Table 3.1. The Damköhler number for the hydrogen-air mixture was calculated to be 2.4, whereas for the methane-air and equimolar mixtures, the values are below unity, at 0.61 and 0.93, respectively.

Table 3.2: Downstream vortex diameter and velocity in three mixtures

Set	Properties	$2H_2 + O_2 + 3.76N_2$	$CH_4 + H_2 + 2.5O_2 + 9.4N_2$	$CH_4 + 2O_2 + 7.52N_2$
1	Flame time (ms)	0.154	0.654	1.41
2	Vortex diameter (mm)	39	39	39
3	Vortex tangential velocity(m/s)	105.8	64	45.2
4	Damköhler number*	2.4	0.93	0.61

From the Borghi regime diagram for premixed turbulent combustion, which attempts to classify turbulent flames into different regimes [23], we can observe that in the region where Da $<$ 1, the chemical reactions are slow compared to the rate at which reactants are being mixed by the flow dynamics. In this region, the integral length scale vortex of the turbulence spectrum, has the capability to disrupt the preheat zone, wrinkle the flame front, and cause local flame quenching [24].

Methane and the equimolar blend are situated in this region. A smaller Damköhler number for the methane mixture leads to more wrinkled structures and local extinction compared to the equimolar blend. Additionally, in the equimolar flame, due to an increase in the mole fraction of hydrogen in the positive curvatures of the flame front compared to its planar form [14], the amount of local quenching induced by turbulence is reduced. As a result, the equimolar mixture recorded a higher normalized pressure than the methane mixture.

On the other hand, for the hydrogen-air mixture with a Damköhler number greater than unity, the flame time was shorter than the characteristic time of the vortical structure. As a result, the flame could withstand the effects of turbulence and was less prone to wrinkling and deformation. The hydrogen flame consumed the vortex rapidly, leading to smaller flame surface enhancement, normalized pressure, and flame tip velocity compared to the methane-air and equimolar blend mixtures.

Chapter 4

Three-Dimensional visualization

4.1 3rd Dimension Visualization

In the second set of experiments, a novel setup was employed to visualize flame propagation in three dimensions as it propagated along the shock tube. To achieve this, two prism mirrors were placed on the top and bottom walls of the shock tube in parallel. The shadowgraph technique was employed to capture the evolution of the flames as they propagated and rolled up into the vortical structures.

The main purpose of these experiments is to enhance the understanding of flame dynamics in all three dimensions and to investigate and compare flame behavior for these three mixtures. By utilizing prism mirrors, the flame's propagation and interaction with the obstacle can be visualized along the width of the shock tube. Selected frames in Figures 4.1 ,4.2, and 4.3 show the flames' evolution.

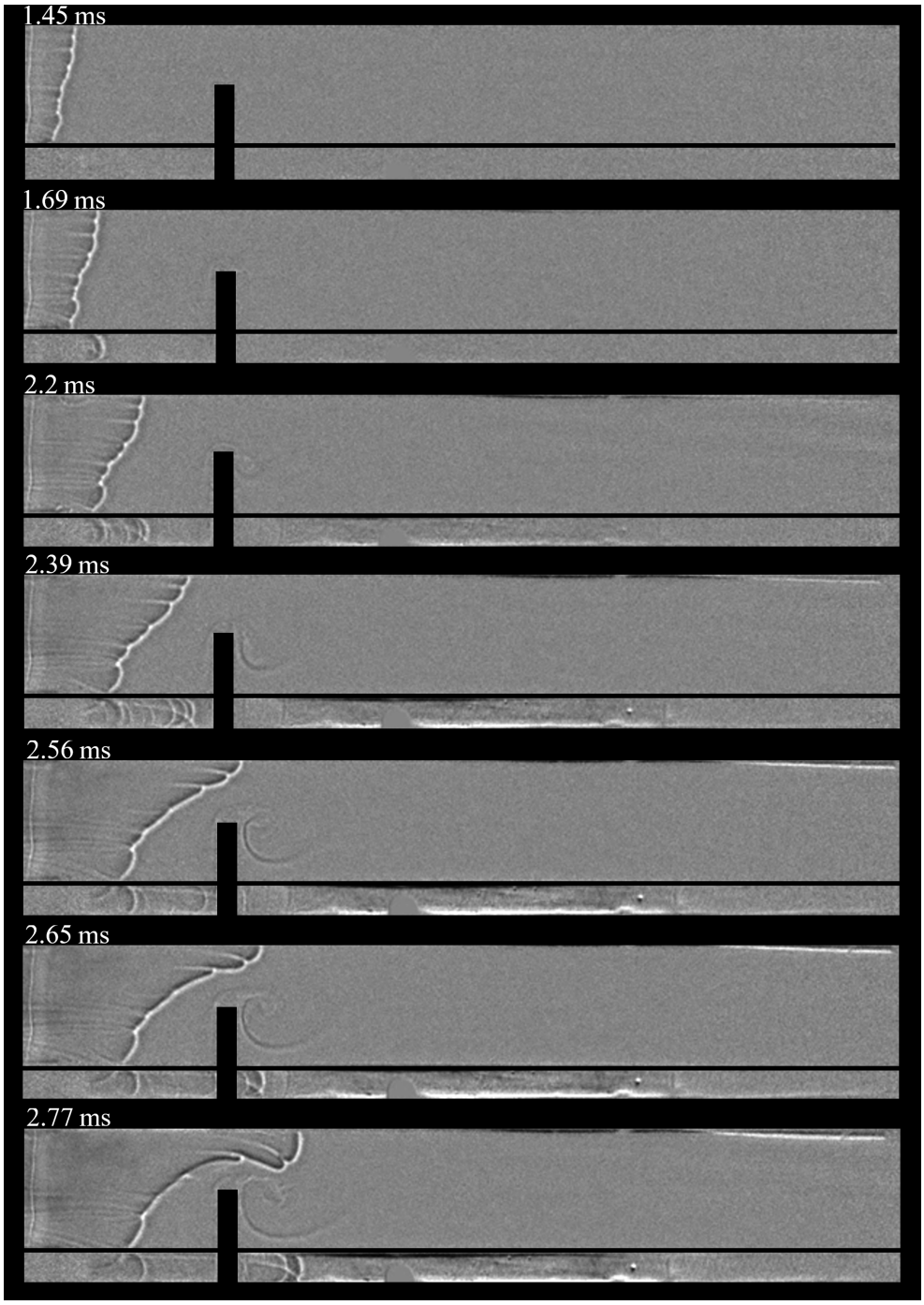
1.45 ms
1.69 ms
2.2 ms
2.39 ms
2.56 ms
2.65 ms
2.77 ms

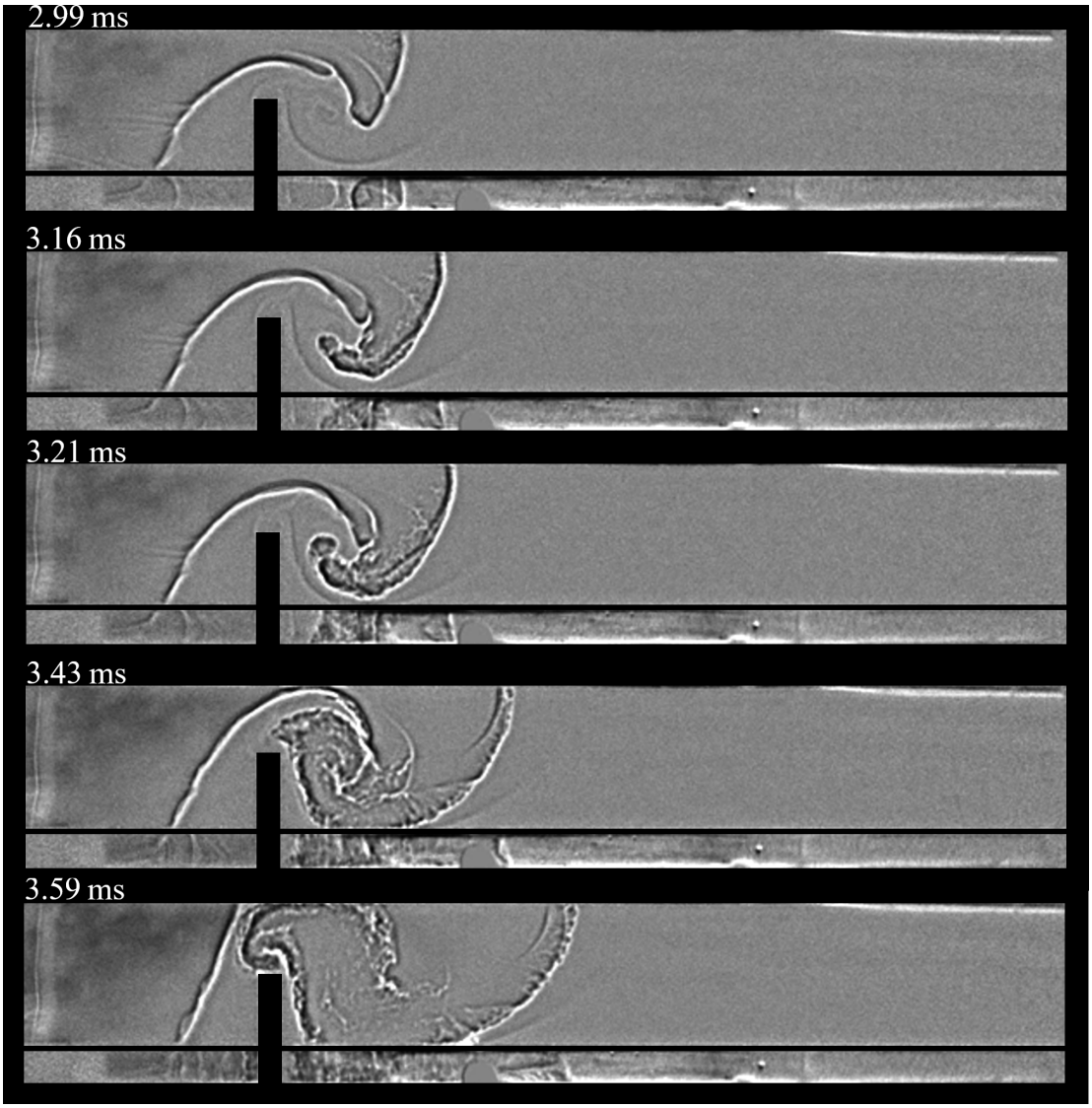
2.99 ms
3.16 ms
3.21 ms
3.43 ms
3.59 ms

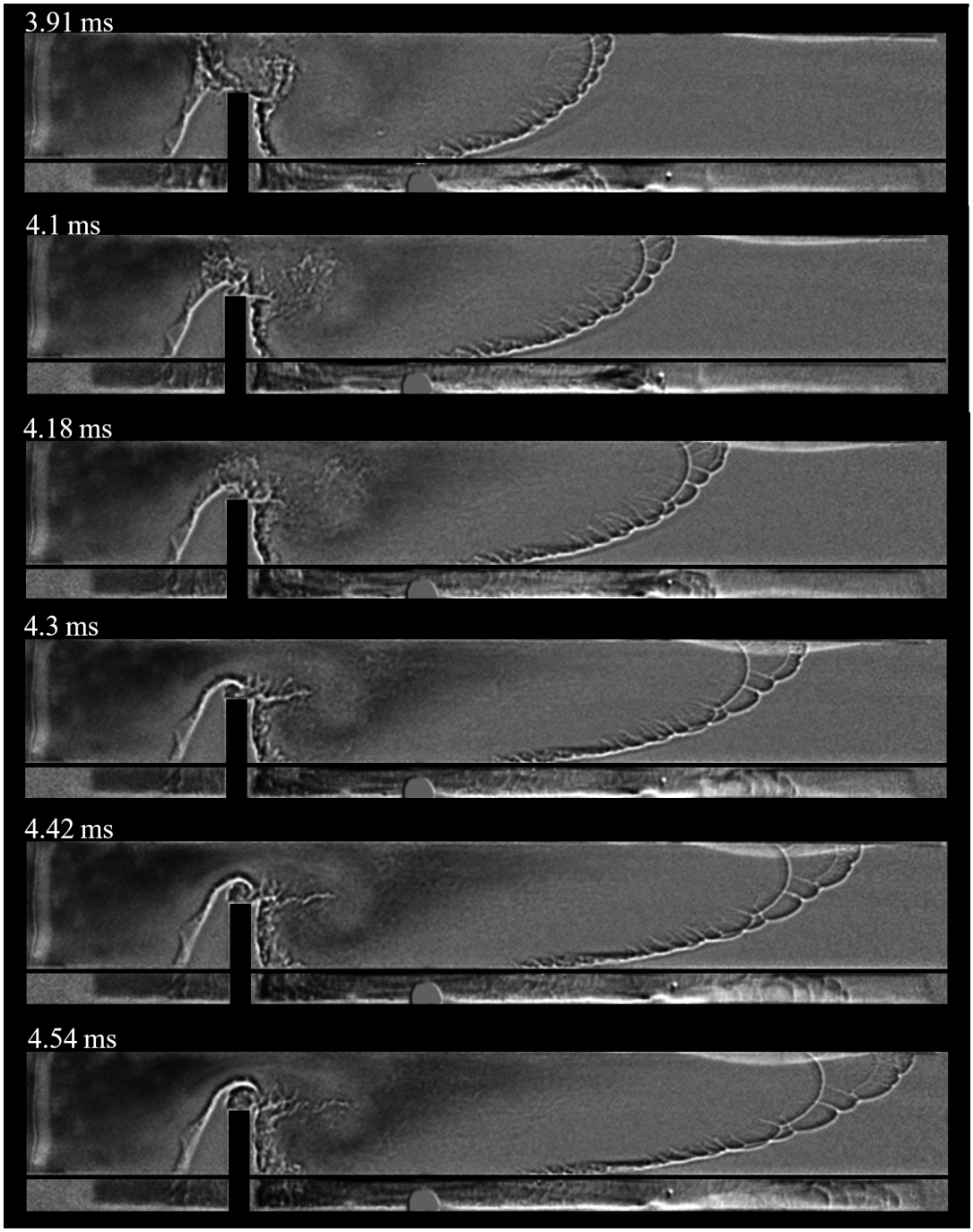

Figure 4.1: Three-dimensional visualization of hydrogen-air flame evolution using shadowgraph technique. Times are shown above each frame and t=0 is the time when the flame ignites.

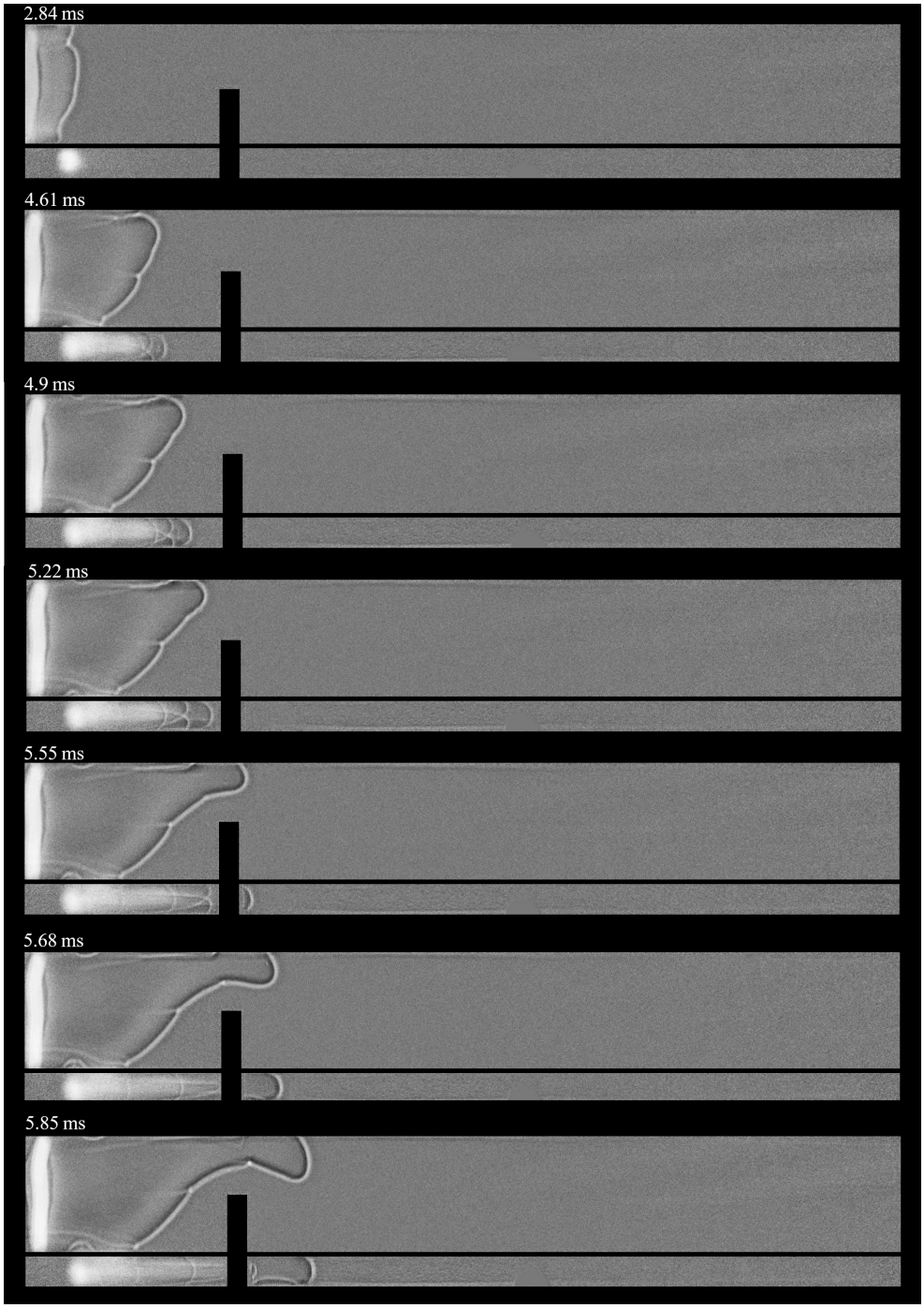
2.84 ms
4.61 ms
4.9 ms
5.22 ms
5.55 ms
5.68 ms
5.85 ms

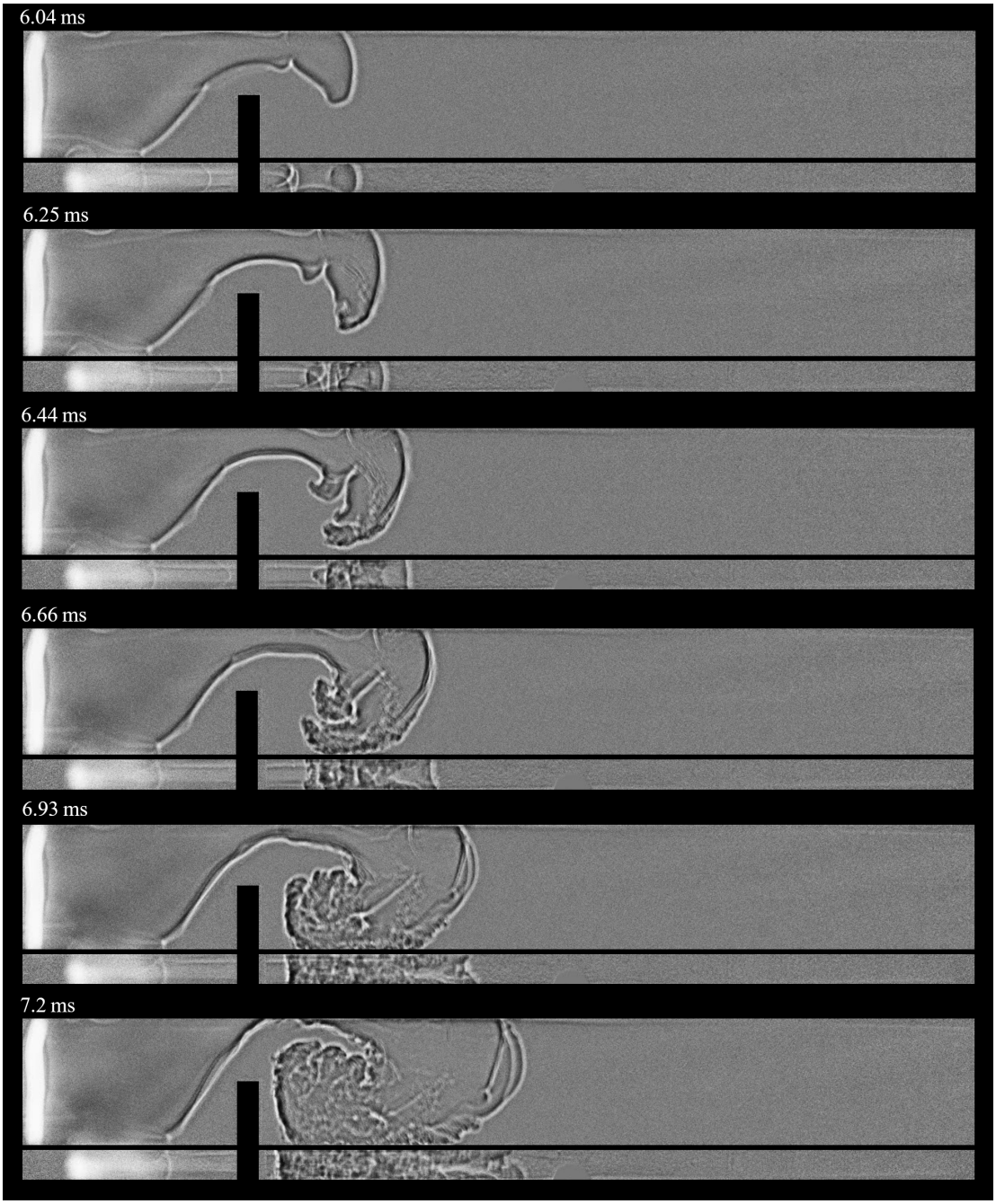
6.04 ms
6.25 ms
6.44 ms
6.66 ms
6.93 ms
7.2 ms

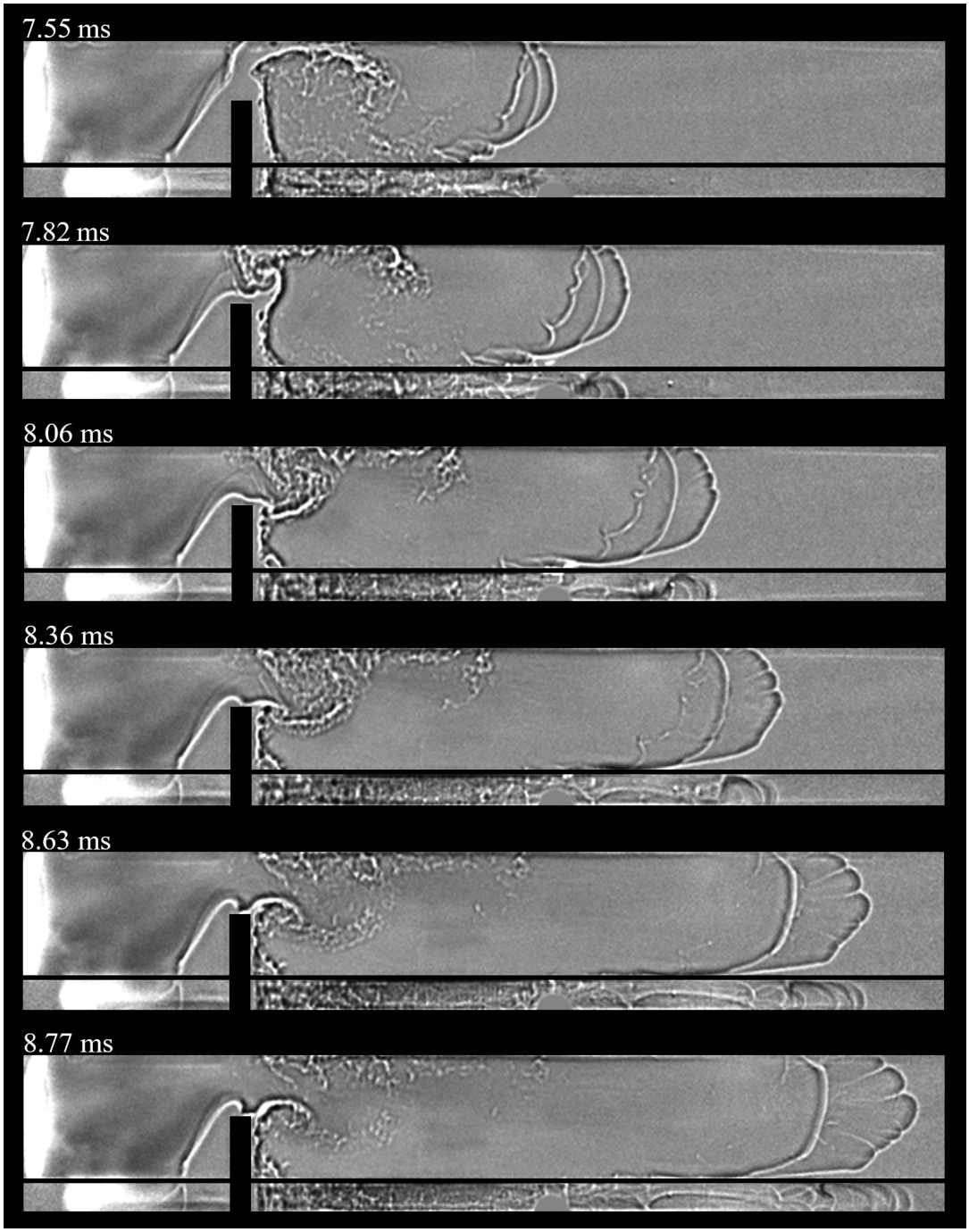

Figure 4.2: Three-dimensional visualization of equimolar blend flame evolution using shadowgraph technique. Times are shown above each frame and t=0 is the time when the flame ignites.

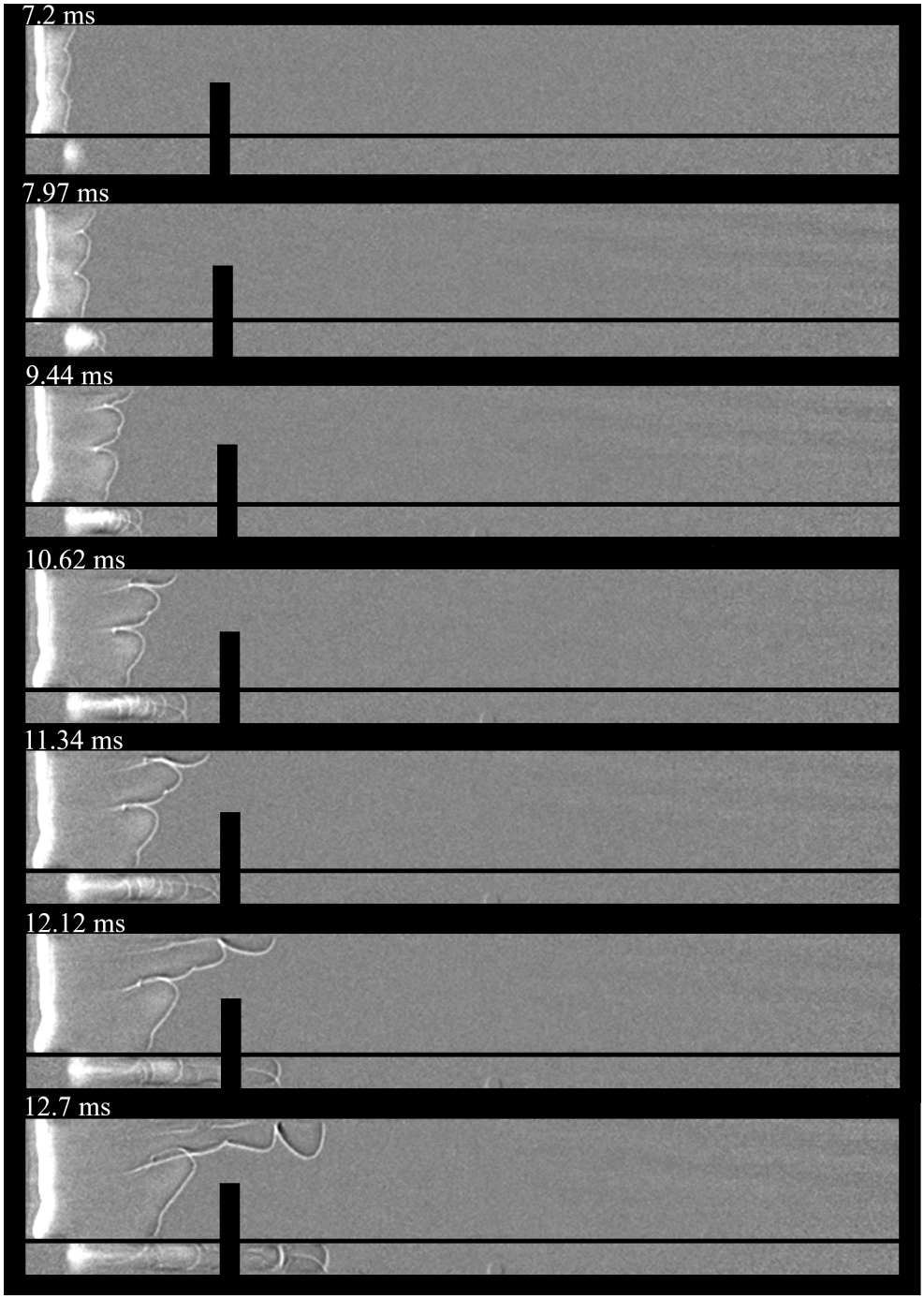
7.2 ms
7.97 ms
9.44 ms
10.62 ms
11.34 ms
12.12 ms
12.7 ms

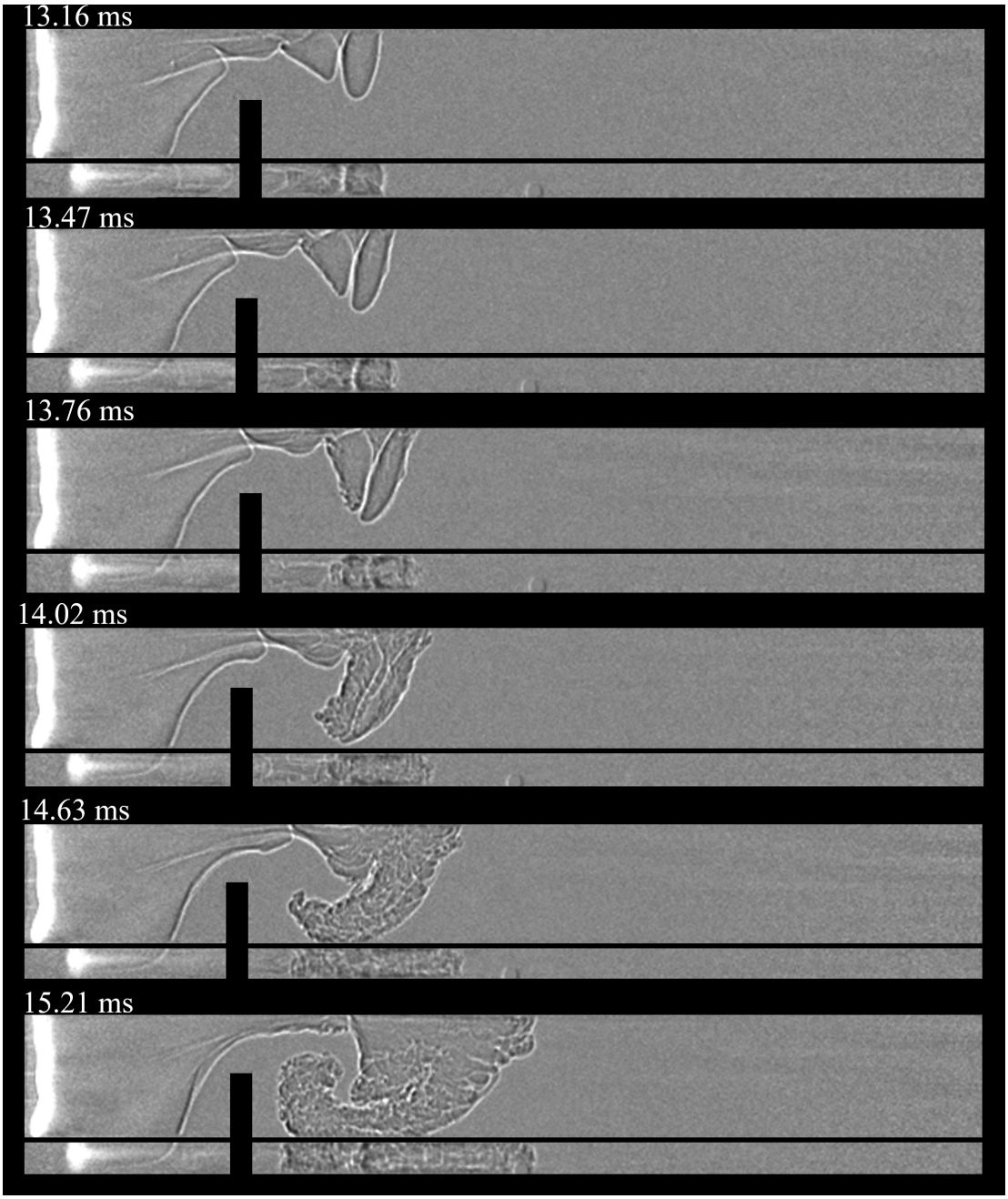
13.16 ms
13.47 ms
13.76 ms
14.02 ms
14.63 ms
15.21 ms

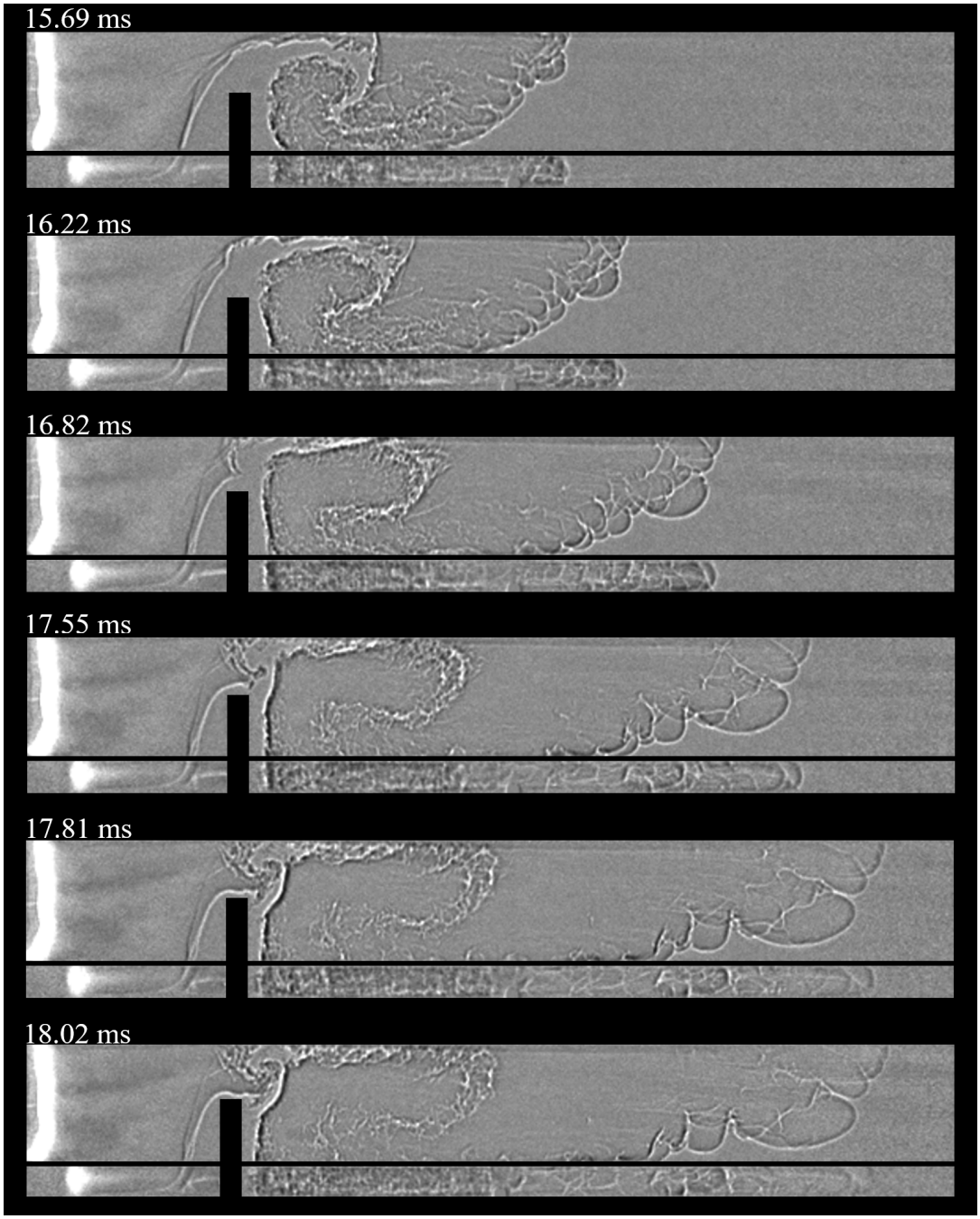

Figure 4.3: Three-dimensional visualization of methane-air flame evolution using shadowgraph technique. Times are shown above each frame and t=0 is the time when the flame ignites.

Selected frames in Figures 4.4 and 4.5 summarize and compare the evolution of the flames as they propagate through the channel.The third dimension of flames evolution can be seen along the bottom row of each frame. It is observed that hydrogen and equimolar mixtures exhibit more 3D effects than methane flames. Hydrogen and equimolar flames tended to incline along the width of the shock tube (appeared as double line in the flame front Figure 4.5) and showed this behavior more intensely when they got entrained into vortical structures and accelerated. On the other hand, the methane flame was less prone to inclining in the third dimension or showing 3D effects, tending to propagate more uniformly compared to the other two.

One possible explanation for this behavior could be the effect of the Lewis number. Hydrogen and equimolar flames, with Lewis numbers below unity, were more prone to show 3D effects compared to methane flames, which have Lewis numbers close to unity [1, 25] (the effective Lewis number will be discussed in Section 4.3).

Dejoan [15] and Kurdyumov [16] studied the propagation of flames in narrow channels for mixtures with Lewis numbers smaller than one. They demonstrated that for Lewis numbers below one, even just slightly below, there is always a critical channel width beyond which the flames tend to exhibit a non-symmetric formation. In our experiments, this non-symmetric shape appeared as an inclination along the width of the shock tube and can be seen clearly in the hydrogen and equimolar mixtures.

4.2 Flame Tip Velocity

Figures 4.6, 4.7, and 4.8 illustrate the evolution of the flame tip velocity over time in the three mixtures. The velocity was measured as the forwardmost flame front location along the horizontal axis in experimental photographs. Each curve has been adjusted in time such that the flame tip crosses the leading edge of the obstacle at $t = 0$. The hydrogen flame propagated significantly faster than the methane flame, while the equimolar blend propagated at a speed in between the two extremes throughout the experiment. Like the results from the experiments presented in chapter 3, there was a gradual increase in velocity for negative times, which was associated with the initial growth of cellular structures. Shortly before time zero, a much sharper increase was observed related to natural contraction and acceleration of downstream flow ahead of the obstacle in vena contracta. When the flames passed through the vena contracta, there was a sudden enlargement in cross-sectional area that caused flow divergence. Due to this flow expansion and flame entrainment in vortices, flame tip velocity decreased for a short period. After that, there was a reactive coupling between the increase in burning rate associated with the enhancement in flame surface area

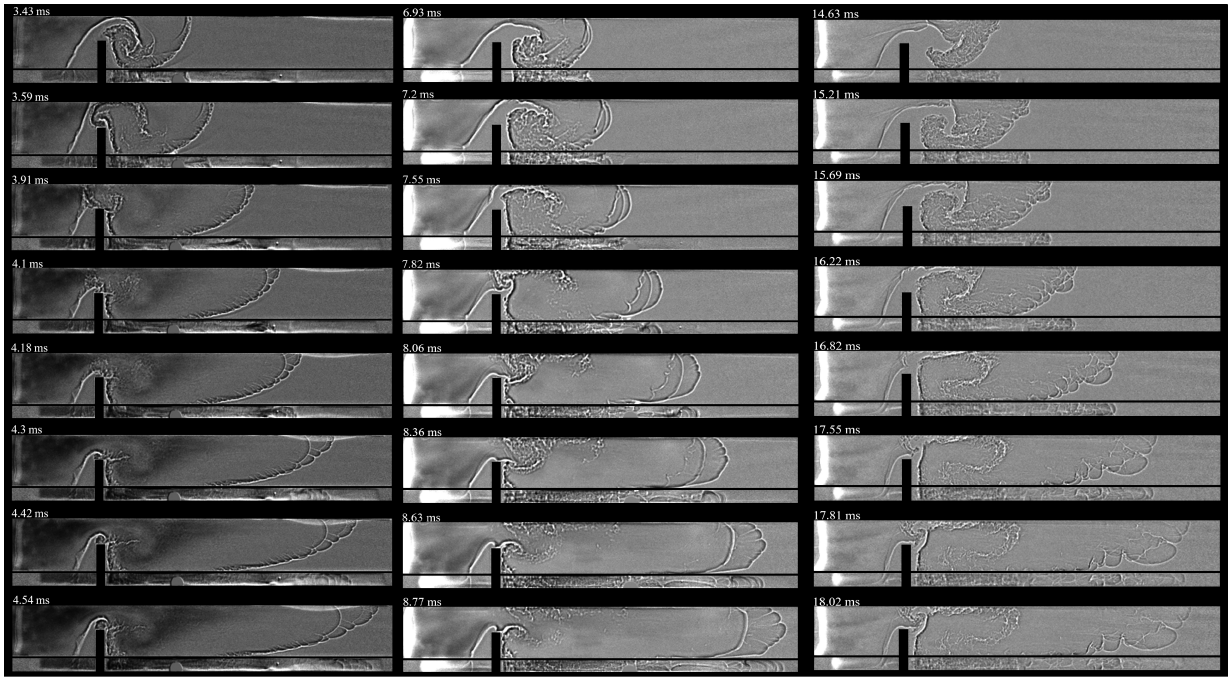

Figure 4.4: Three-dimensional visualization the flames evolution using shadowgraph technique. Times are shown above each frame and t=0 is the time when the flame ignites.

resulting from the flame roll-up, and the strong acceleration of flow induced ahead of the flame by the rapid expansion of the burned gases and flame acceleration.

To compare the flame tip velocity between the results of two sets of experiments (Figures 4.6, 4.7, and 4.8), the new oblique top and bottom walls in the 3D visualization experiments increased the effect of the boundary layer. Consequently, the flame tip velocity in all three mixtures was lower than in the experiments without prism mirrors during flame propagation, and the flame rolled up into the vortices inside the shock tube.

In the experiments presented in chapter 3, the first velocity peaks were approximately 270 m/s for hydrogen, 130 m/s for the equimolar blend, and 80 m/s for methane. These values fell to 175 m/s, 95 m/s, and 50 m/s, respectively, in the experiments with prism mirrors. Additionally, the time it took for the flame to travel through the shock tube increased in all three mixtures during the 3D visualization experiments. However, the maximum flame tip velocities after flame roll-up into the vortical structures and subsequent acceleration were comparable for all three mixtures in both sets of experiments. This

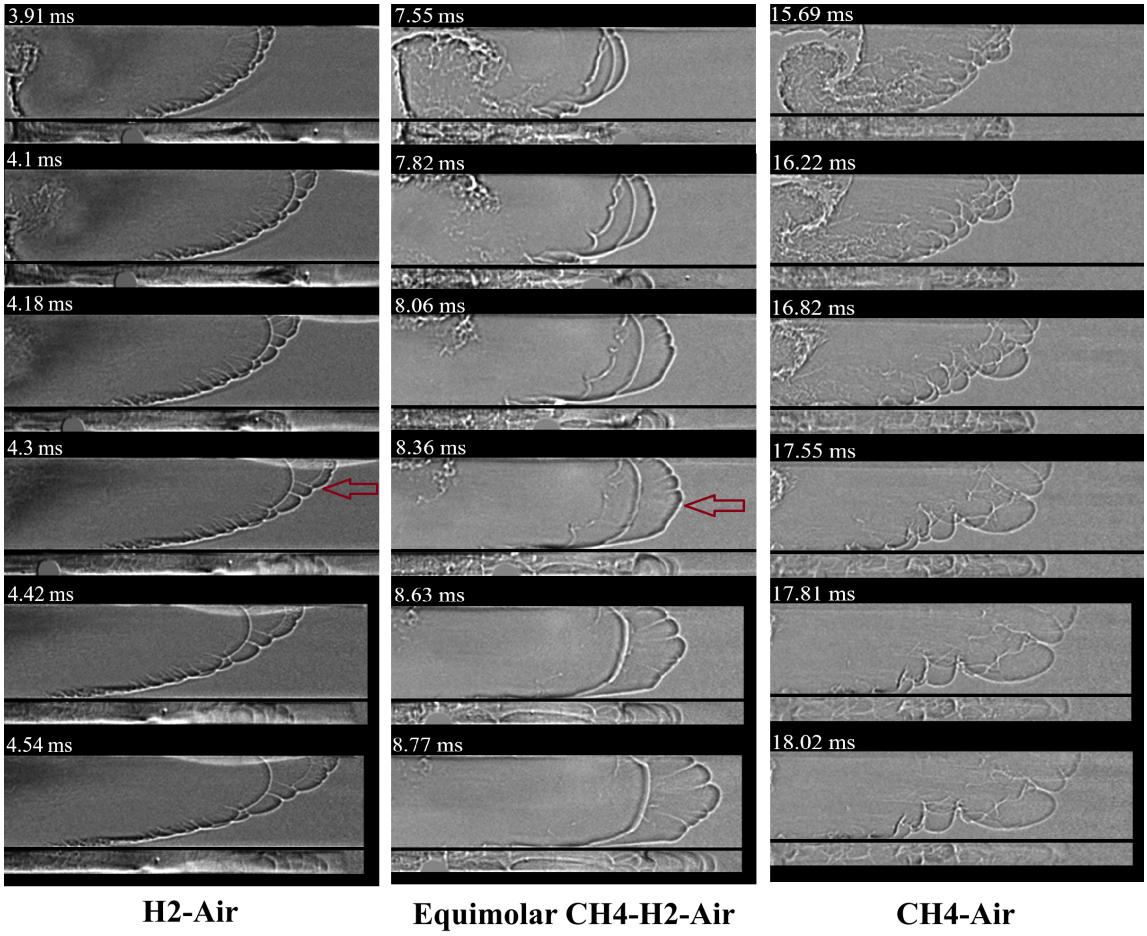

Figure 4.5: Three-dimensional visualization of the selected frames shown in a closer view.

indicates that the effects of flame entrainment in vortices and the associated acceleration due to area enhancement outweighed the effect of the boundary layer.

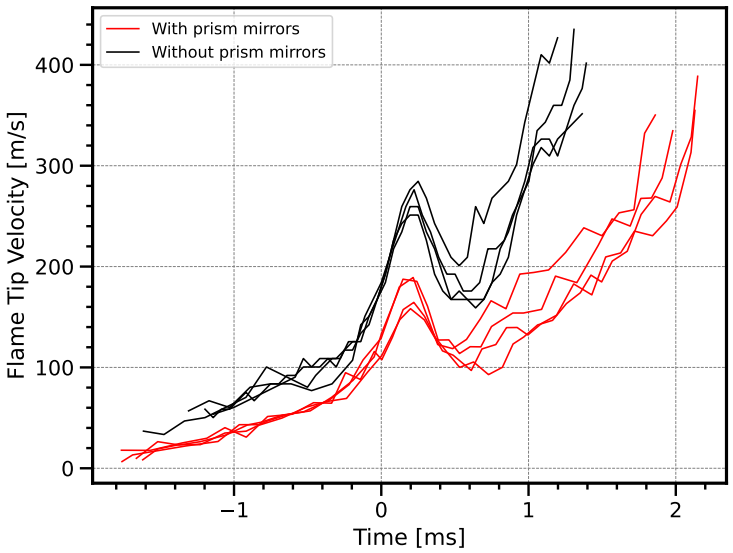

Figure 4.6: Evolution of the flame tip velocity for hydrogen-air flame over time. Time $t = 0$ is defined as the moment when the flame tip crosses the leading edge of the obstacle.

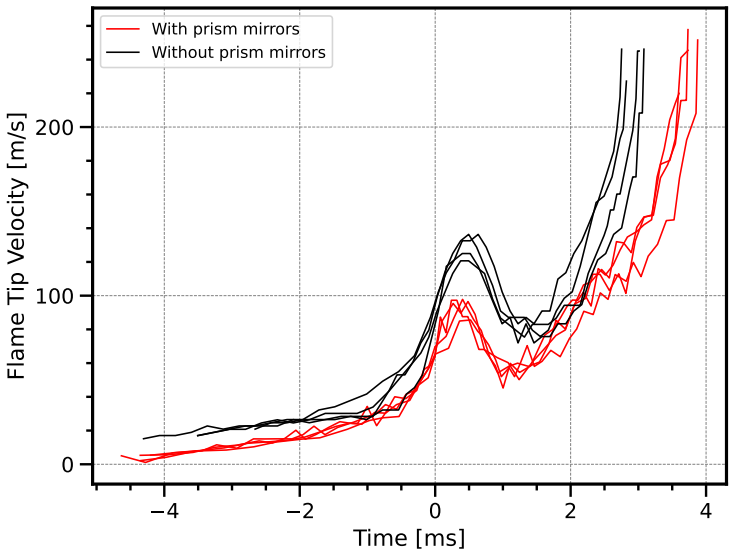

Figure 4.7: Evolution of the flame tip velocity for blend-air flame over time. Time $t = 0$ is defined as the moment when the flame tip crosses the leading edge of the obstacle.

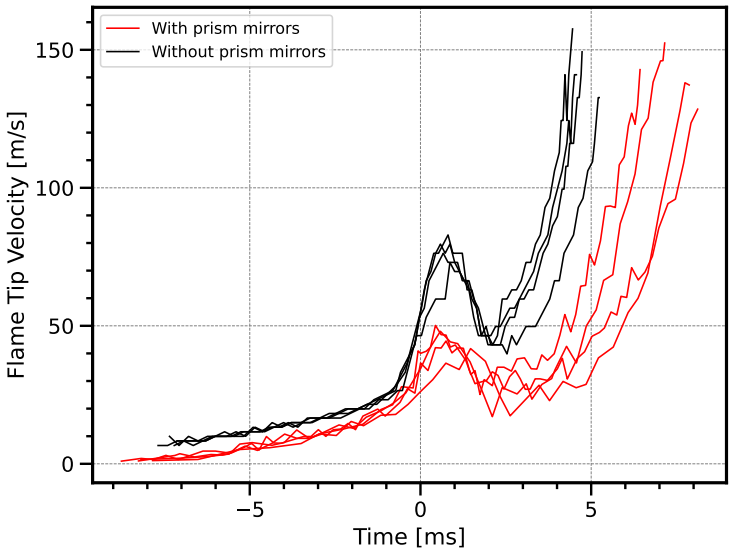

Figure 4.8: Evolution of the flame tip velocity for methane-air flame over time. Time $t = 0$ is defined as the moment when the flame tip crosses the leading edge of the obstacle.

4.3 Effect of Lewis number on flame deformation in the 3rd dimension

The experimental results presented in Section 4.1 demonstrate that hydrogen and equimolar flames exhibit more pronounced 3D effects than the methane flame. Hydrogen and equimolar flames tended to incline along the width of the shock tube (appearing as a double line in the flame front, see Figure 4.5), and this behavior intensified when the flames got entrained into vortical structures and accelerated. In contrast, the methane flame was less prone to inclining in the third dimension. One possible explanation for this behavior could be the effect of Lewis number. To better understand how to estimate the Lewis number for hydrogen/methane fuel blends, we can refer to the work conducted by Bouvet et al. [1].

They investigated the equivalent formulations for the effective Lewis number in bi-component fuels, such as hydrogen/hydrocarbon fuel blends. The mixtures' Lewis numbers are calculated using the effective formulations Le_H, Le_V, and Le_D (Table 4.1).

We can see from all three approaches (represented in Figure 4.9) that the Lewis number for hydrogen/hydrocarbon fuel blends with varying compositions falls between the Lewis numbers of hydrogen–air and hydrocarbon–air flames. Based on this observation and considering that the Lewis number is close to unity for the methane–air flame and below

unity for the hydrogen–air flame, we can conclude that the Lewis number for the equimolar flame is also below unity. In this context, one possible explanation for the inclination of hydrogen and equimolar flames in the third dimension is that they possess a Lewis number below unity and tend to reinforce their positive curvature along the width of the shock tube. This behavior causes the flame front to appear as a double line; see Figure 4.5.

Positive curvature toward unburned gas in the reaction sheet serves as a local sink for reactants and a local source for heat. Increasing the rate of diffusion of the limiting reactant to the flame sheet increases the rate of heat release there and hence tends to increase the flame temperature. If the thermal diffusivity is less than mass diffusivity (Le < 1), then the flame temperature increases (as a consequence of the preferential diffusion of the reactant with respect to heat). In this situation, the local increase in the flame speed, associated with the increase in the flame temperature, causes the positive curvature of the flame front to become larger for mixtures with Le< 1 [3].

Table 4.1: Effective Lewis number formulation for bi-component fuels [1]

Effective Lewis number		
Heat release-based (H)	$Le_H = 1 + \frac{q_1(Le_1 - 1) + q_2(Le_2 - 1)}{q_1 + q_2}$	Heat release formulation
Volume-based (V)	$Le_V = X_1 Le_1 + X_2 Le_2$	Volumetric fraction-weighted
Diffusion-based (D)	$Le_D = \frac{D_T}{X_1 D_{1/N_2} + X_2 D_{2/N_2}}$	Diffusion formulation

D_T, the mixture thermal diffusivity and $D_{i/N2}$, the mass diffusivity of the deficient fuel species i

The first expression in Table 4.1, which is a weighted average of the Lewis numbers of the two fuels based on their respective non-dimensional heat release, was introduced by Law et al. [26]. This expression was presented in their investigation of the cellular instability of high-pressure H_2/C_3H_8 laminar spherical flames. Furthermore, this formulation was extended to three fuel species [27] to comment on the thermodiffusive stable (Le > 1) or unstable (Le < 1) character of H_2/HC/air flames.

Muppala et al. [28, 29] used the volumetric fraction-weighted average formulation in Table 4.1. When applied in their chosen flame surface wrinkling model this calculation showed fair agreement with experimental burning velocities. However, it is important to note a progressive underestimation at higher turbulent intensities.

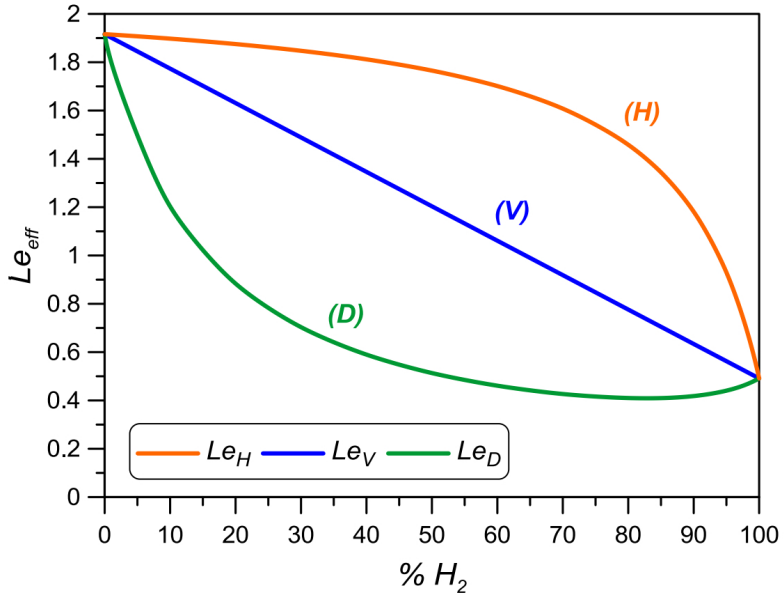

Figure 4.9: Effective Lewis number formulations for H_2/C_3H_8/air flames versus H_2 fuel volumetric content [1]

Dinkelacker et al. [30, 31] investigated the third effective Lewis number approach in Table 4.1. If positively curved flame elements dominate turbulent flame propagation, it was hypothesized that the leading edge of the flame would be enriched in the most diffusive fuel. Consequently, the resulting effective Lewis number should depend on a volumetric fraction-weighted average of the fuel diffusivities.

The volumetric weighted approach, Le_V, was found to be the most consistent one for the tested alkanes (CH_4, C_3H_8 and C_8H_{18}). However, the Le_V formulation could not be confirmed for syngas mixtures. In this case, the Markstein length, and therefore flame stability, are expected to be influenced by detailed chemical effects that cannot be considered in classical one-step chemistry models [1].

The heat release formulation, Le_H, seems to overweight the hydrocarbon influence on the H_2/HC flame stability characteristics. The diffusion formulation, Le_D, is found to clearly overweight the hydrogen influence on the H_2/HC flame stability characteristics [1].

Chapter 5

Conclusion

Experiments were conducted to characterize the differences between flames propagating in stoichiometric mixtures of hydrogen, methane, and an equimolar hydrogen-methane blend with air. With a bluff body obstacle present downstream and a flame-driven flow, vortical structures formed ahead of the flame. The subsequent interaction of the flame with these vortices generated substantial flame area enhancement and acceleration. The measured evolution of the flame velocity and overpressure inside the shock tube highlighted the higher flame acceleration and overpressure of the hydrogen-air flame due to its higher burning velocity compared to the flames propagating in methane-air and equimolar blend. The pressure and flame tip velocity measured in the equimolar blend fell somewhere between these two extreme mixtures.

In this study, the velocity and pressure evolution inside the shock tube were investigated non-dimensionally. To eliminate the dependency of the measured flame tip velocity and pressure on the flame's chemistry and properties, these data were presented in non-dimensional form. The pressure and velocity were normalized by $\rho_u \sigma^2 S_L^2$ and σS_L respectively to account for the distinct laminar burning velocities of each mixture. Interestingly, the equimolar blend mixture had the highest normalized velocity and overpressure, followed by the methane mixture. The hydrogen mixture exhibited the lowest scaled velocity and overpressure inside the shock tube. These results illustrated that the hydrogen flame had a smaller surface area enhancement compared to the methane and equimolar blend flames. Hydrogen-air has a much shorter flame time compared to the other mixtures, allowing it to consume flame folds more quickly. This results in less surface area enhancement, as the smaller folds were used up faster than they can expand, and the increase in surface area was thus mainly due to the deformation of the larger scales of the flame surface. In the other mixtures, the efficient folding of the flame surface at smaller scales also contributed

to their larger surface areas, as the consumption of these folds could not keep pace with their growth.

These three flames interacted differently with vortical structures. The hydrogen-air flame as a reactive fuel, with smaller flame time compared to the other mixtures, consumed the vortex rapidly as rolled up into it. It was less prone to disturb by vortex and turbulent shear layer above the obstacle. In contrast, vortices disturbed and broke the flame structure in methane and equimolar mixtures, causing these flames to get entrained into them for a longer time, which was visible in the experimental photographs. This behavior highlighted the importance of the characteristic time of the flames, the characteristic time of the vortex, and the relation between them.

The relation between the characteristic time of the flame and flow dynamics appeared to govern the flame's behavior in terms of vortex entrainment. For methane and equimolar mixtures with a Damköhler number less than unity, all the eddies, including the length scale vortex of the turbulence spectrum, had the capability to disrupt the preheat zone and wrinkle the flame front area. On the other hand, for the hydrogen-air mixture with a Damköhler number greater than unity, the flame time was shorter than the characteristic time of the vortical structure. As a result, the flame could withstand the effects of turbulence and was less prone to wrinkling and deformation. This leaded to a smaller flame surface enhancement, normalized pressure, and flame tip velocity compared to the methane and the equimolar blend mixtures.

The higher normalized pressure and flame tip velocity of the equimolar flame, compared to that of the methane flame, highlighted the importance of preferential diffusion of reactants in a two-reactant system. In the equimolar flame, due to an increase in the concentration of hydrogen as a more strongly diffusing reactant, in the positive curvatures of the flame front compared to its planar form, the amount of local quenching induced by turbulence was reduced. As a result, the equimolar mixture recorded a higher normalized overpressure than the methane mixture.

A novel method was established to visualize the flames three-dimensionally. In the 3D visualization experiments, hydrogen and equimolar flames showed more 3D effects than the methane flame. Hydrogen and equimolar flames tended to incline along the width of the shock tube and exhibited this behavior more intensely when they got entrained into the vortical structures and accelerated. On the other hand, the methane flame was less prone to inclining and tended to propagate more uniformly in the third dimension compared to the other mixtures.

These results indicated that the higher normalized pressure and flame tip velocity in the methane and equimolar blend flames were not due to the 3D effect, as the hydrogen flame exhibited greater 3D effects, but had lower normalized pressure and flame tip velocity compared to the methane flame. This suggests that the Damköhler number has a more significant impact than the Lewis number.

References

[1] N.Bouvet, F.Halter, C.Chauveau, and Y.Yoon. On the effective Lewis number formulations for lean hydrogen/hydrocarbon/air mixtures. *International Journal of Hydrogen Energy*, 38:5949–5960, 2013.

[2] C.K.Law. *Combustion Physics*. Cambridge University Press, 2010.

[3] F.A.Williams. *Combustion Theory*. Westview Press, 2nd edition, 1985.

[4] M.Gharib, E.Rambod, and K.Shariff. A universal time scale for vortex ring formation. *Journal of Fluid Mechanics*, 360:121–140, 1998.

[5] G.S.Settles. *Schlieren and Shadowgraph Techniques: Visualizing Phenomena in Transparent Media*. Springer, 2001.

[6] B.T.Chu. On the generation of pressure waves at a plane flame front. *Cellular Flames and Oscillatory Combustion*, 77:603–612, 1953.

[7] N.Peters. Length scales in laminar and turbulent flames. Numerical approaches to combustion modeling. *Progress in Astronautics and Aeronautics*, 135:155–182, 1991.

[8] G.H.Markstein. *Nonsteady Flame Propagation*, volume 75. Pergamon Press, 1964.

[9] G.I.Sivashinsky. Diffusional-thermal theory of cellular flames. *Combustion Science and Technology*, 15:137–145, 1977.

[10] G.Darrieus. Propagation d'un front de flamme. *La Technique Moderne*, 1938.

[11] L.D.Landau. On the theory of slow combustion. *Acta Physicochimica URSS*, 19:77–85, 1945.

[12] C.T.Johansen and G.Ciccarelli. Visualization of the unburned gas flow field ahead of an accelerating flame in an obstructed square channel. *Combustion and Flame*, 156:405–416, 2009.

[13] W.L.Roberts, J.F.Driscoll, M.C.Drake, and L.P.Goss. Images of the quenching of a flame by a vortex to quantify regimes of turbulent combustion. *Combustion and Flame*, 94:58–69, 1993.

[14] S.Shi, A.Breicher, R.Schultheis, S.Hartl, R.S.Barlow, D.Geyer, and A.Dreizler. Structures of laminar lean premixed H2/CH4/air polyhedral flames: Effects of flow velocity, H2 content and equivalence ratio. *Flow, Turbulence and Combustion*, 113:1081–1110, 2024.

[15] A.Dejoan, C.Jiménez, and V.N.Kurdyumov. Critical conditions for non-symmetric flame propagation in narrow channels: Influence of the flow rate, the thermal expansion, the Lewis number and heat-losses. *Combustion and Flame*, 209:430–440, 2019.

[16] V.N.Kurdyumov. Lewis number effect on the propagation of premixed flames in narrow adiabatic channels: Symmetric and non-symmetric flames and their linear stability analysis. *Combustion and Flame*, 158:1307–1317, 2011.

[17] G.Pizza, C.E.Frouzakis, J.Mantzaras, A.G.Tomboulides, and K.Boulouchos. Dynamics of premixed hydrogen/air flames in mesoscale channels. *Combustion and Flame*, 155:2–20, 2008.

[18] G.Pizza, C.E.Frouzakis, J.Mantzaras, A.G.Tomboulides, and K.Boulouchos. Dynamics of premixed hydrogen/air flames in microchannels. *Combustion and Flame*, 152:433–450, 2008.

[19] Y.Ju and B.Xu. Effects of channel width and Lewis number on the multiple flame regimes and propagation limits in mesoscale. *Combustion Science and Technology*, 178:1723–1753, 2006.

[20] C.Cui, M.Matalon, J.Daou, and J.Dold. Effects of differential diffusion on thin and thick flames propagating in channels. *Combustion Theory and Modeling*, 8:41–64, 2004.

[21] D.F.Galisteo, A.Dejoan, J.M.Gavilanes, and V.N. Kurdyumov. A three-dimensional study of the influence of momentum loss on hydrodynamically unstable premixed flames. *Proceedings of the Combustion Institute*, 39:1545–1554, 2023.

[22] M.J.Hargather and G.S.Settles. Retroreflective shadowgraph technique for large-scale flow visualization. *Applied Optics*, 48:4449–4457, 2009.

[23] R.W.Borghi. On the structure and morphology of turbulent premixed flames. *Recent Advances in the Aerospace Sciences*, pages 117–138, 1985.

[24] P.H.Renard, D.Thévenin, J.C.Rolon, and S.Candel. Dynamics of flame/vortex interactions. *Progress in Energy and Combustion Science*, 26:225–282, 2000.

[25] G.O.Erol, M.Klein, and N.Chakraborty. Lewis number effects on flame speed statistics in spherical turbulent premixed flames. *Flow, Turbulence and Combustion*, 106:1043–1063, 2021.

[26] C.K.Law, G.Jomaas, and J.K.Bechtold. Cellular instabilities of expanding hydrogen/propane spherical flames at elevated pressures: Theory and experiment. *Proceedings of the Combustion Institute*, 30:1477–1484, 2005.

[27] T.M.Vu, J.Park, O.B.Kwon, and J.S.Kim. Effects of hydrocarbon addition on cellular instabilities in expanding syngas-air spherical premixed flames. *International Journal of Hydrogen Energy*, 34:6961–6969, 2009.

[28] S.P.R.Muppala, M.Nakahara, N.K.Aluri, H.Kido, J.X.Wen, and M.V.Papalexandris. Experimental and analytical investigation of the turbulent burning velocity of two-component fuel mixtures of hydrogen, methane and propane. *International Journal of Hydrogen Energy*, 34:9258–9265, 2009.

[29] S.P.R.Muppala, N.K.Aluri, F.Dinkelacker, and A.Leipertz. Development of an algebraic reaction rate closure for the numerical calculation of turbulent premixed methane, ethylene, and propane/air flames for pressures up to 1.0 MPa. *Combustion and Flame*, 140:257–266, 2005.

[30] F.Dinkelacker, B.Manickam, and S.P.R.Muppala. Modelling and simulation of lean premixed turbulent methane/hydrogen/air flames with an effective Lewis number approach. *Combustion and Flame*, 158:1742–1749, 2011.

[31] F.Dinkelacker. Why the Lewis number seems to have an unexpected importance even in highly turbulent flames. *11th International Workshop on Premixed Turbulent Flames*, 2008.